Mathematical Formulation of the Remote Electric and Magnetic Emissions of the Lightning Dart Leader and Return Stroke

by

Edward M. B. Thiemann

B.S. University of Colorado, 2007

M.S. Georgia Institute of Technology, 2009

A thesis submitted to the Faculty of the Graduate School of the University of Colorado in partial fulfillment of the requirement for the degree of

Master of Engineering

Department of Electrical, Computer and Energy Engineering

2013

This thesis entitled:
Mathematical Formulation of the Remote Electric and Magnetic Emissions of the
Lightning Dart Leader and Return Stroke
written by Edward M. B. Thiemann
has been approved for the Department of Electrical, Computer and Energy Engineering

_____
Albin J. Gasiewski

_____
Nikolay A. Zabotin

Date _____

The final copy of this thesis has been examined by the signatories, and we
Find that both the content and the form meet acceptable presentation standards
Of scholarly work in the above mentioned discipline.

Thiemann, Edward M.B. (M.Eng., Electrical, Computer and Energy Engineering)

Mathematical Formulation of the Remote Electric and Magnetic Emissions of the Lightning Dart Leader and Return Stroke

Thesis directed by Professor Albin J. Gasiewski

Lightning detection and geolocation networks have found widespread use by the utility, air traffic control and forestry industries as a means of locating strikes and predicting imminent recurrence. Accurate lightning geolocation requires detecting VLF radio emissions at multiple sites using a distributed sensor network with typical baselines exceeding 150 km, along with precision time of arrival estimation to triangulate the origin of a strike. The trend has been towards increasing network accuracy without increasing sensor density by incorporating precision GPS synchronized clocks and faster front-end signal processing. Because lightning radio waveforms evolve as they propagate over a finitely conducting earth, and that measurements for a given strike may have disparate propagation path lengths, accurate models are required to determine waveform fiducials for precise strike location. The transition between the leader phase and return stroke phase may offer such a fiducial and warrants quantitative modeling to improve strike location accuracy.

The VLF spectrum of the ubiquitous downward negative lightning strike is able to be modeled by the transfer of several Coulombs of negative charge from cloud to ground in a two-step process. The lightning stepped leader ionizes a plasma channel downward from the cloud at a velocity of approximately 0.05c, leaving a column of charge in its path. Upon connection with a streamer, the subsequent return stroke initiates at or near ground level and travels upward at an average but variable velocity of 0.3c. The return stroke neutralizes any negative charge along its path. Subsequent dart leader and return strokes often travel smoothly down the heated channel left by a preceding stroke, lacking the halting motion of the preceding initial stepped leader and initial return stroke. Existing lightning models often neglect the leader current and rely on approximations when solving for the return stroke.

In this Thesis, I present an analytic solution to Maxwells Equations for the lightning leader followed by a novel return stroke model. I model the leader as a downward propagating boxcar function of uniform charge density and constant velocity, and the subsequent return stroke is modeled as an upward propagating boxcar with a time dependent velocity. Charge conservation is applied to ensure self-consistency of the driving current and charge sources, and physical observations are used to support model development. The resulting transient electric and magnetic fields are presented at various distances and delay times and compared with measured waveforms and previously published models.

Contents

List of Figures

Chapter 1

Introduction

This thesis began as semester project investigating lightning geolocation techniques with an interest towards using lightning location data to estimate the location of wildfire starts. This is the same motivation that spurred the Bureau of Land Management to develop large scale lightning detection networks in the United States in the 1970s. In principle, lightning location data can be used in conjunction with an aerial sensor mounted on an aircraft or drone to investigate possible lightning fires; but because lightning fires can smolder undetected for days, the sensors will need to resolve an area of a few meters to thermally detect a smoldering tree or duff which may not have any flames or a plume visible from above the canopy. Higher accuracy lightning data will improve the efficiency at which an aerial sensor determines whether a particular strike has started a small fire. This initial research revealed that the current accuracy of commercial lightning locating networks was 500-1000 m diameter with the limitations resulting from longer sensor baselines, the sensor bandwidth, and signal processing techniques which matched waveforms measured by different sensors with a particular strike. Since both sensor bandwidth and signal processing depend on lightning emissions; modeling lightning emissions became the focus of my research with the end goal being an independently derived lightning model which is consistent with Maxwell's Equations and depends on parameters taken from lightning observations.

This thesis begins by reviewing the major processes which occur during a lightning strike. Measurements of lightning cloud charge and lightning strike properties such as current and velocity are reviewed next because they are used as model inputs. The model begins by defining the charge and current of a lightning leader as being a vertically propagating box car function over a grounded plane. Maxwell's Equations are solved for this configuration and results are presented in closed form. The lightning return stroke is also solved, but a closed form solution is not possible due to the mathematical form of the velocity. The model for the complete strike is then compared with existing models as well as measured lightning waveforms.

1.1 Overview of Lightning Processes and Terminology

Lightning strikes are typically classified by the propagation direction of the initial charge structure, known as the leader, and the net charge transferred to ground. This results in a total of four possible lightning strikes: downward negative, downward positive, upward negative and upward positive. For most flat geographies, downward initiated lightning is the most common with upward initiated lightning only occurring from tall structures or mountain tops. With regard to downward initiated lightning, the downward negative type strike is far more common, with studies showing that 90% of all lightning strikes are downward negative [31].

The following qualitative description is with regard to downward negative lightning but it can be expanded to upward and/or positive lightning straightforwardly. A lightning *strike* consists of 2 components, the first being the *leader* which is followed by the *return stroke*. A typical lightning *flash* consists of 3-5 strikes occurring over the period of 200-300 ms [31]. The initial leader in a flash is commonly referred to as a *stepped* leader because it propagates through virgin air in a halting (or stepped) fashion and may branch repeatedly. The leader serves as a conducting path between cloud and ground, and once contact with ground is made, the strike enters the return stroke phase as current flows freely along the channel defined by the leader until the leader charge is neutralized. In the case of a downward negative strike, the leader leaves negative charge along the channel and the return stroke neutralizes this with positive charge sourced from ground. Once the leader charge is neutralized by the return stroke, the process, which typically takes tens of microseconds, may end. However, more commonly, subsequent strikes occur and/or *continuing currents* may be initiated [32].

Subsequent strikes are initiated by *dart* leaders which are named in contrast to their branching counterparts, the stepped leader. The hot column of air left by the preceding return strike is partially thermally ionized and has a conductivity of 0.02 S/m (air at sea level has conductivity 10-14 S/m) [32] which gives the subsequent leader a preferred path to follow. This preferred path to ground allows the dart leader to propagate in the straight and un-halting fashion for which it is named. Dart leaders may diverge from the existing channel becoming *dart-stepped* leaders with a different ground termination although this is less common. Once the dart leader makes contact with ground, a subsequent return stroke is initiated which neutralizes the charge left by the dart leader.

Continuing currents occur when the process does not end with the neutralization of leader channel charge by the return stroke. What may happen instead is charge may flow from the cloud down the return stroke path. This occurs during approximately 30-50% of negative lightning flashes and more frequently for positive lightning flashes [32]. The magnitude of continuing currents is 10-100 times smaller than the return stroke peak current and may last from 40-500 ms. Typically, the continuing current magnitude remains constant

but it may surge; these surging components are known as *M-Components*. Continuing currents will not be considered in this thesis but they have practical importance because they are often associated with lightning fire ignitions.

Table 1.1 was taken directly from [31] and shows empirically derived lightning parameters taken by Berger from over 20 years of channel base-current measurements from instrumented towers. It includes typical values for the aforementioned lightning processes and is considered to be the most complete and continuous data set for lightning base current measurements. However, because these measurements were taken from instrumented towers, they reflect statistics associated with lightning strikes to tall objects which may or may not be accurate for lightning strikes to flat areas.

Parameters	Units	Sample size	Percentage exceeding tabulated value		
			95%	50%	5%
Peak current (minimum 2 kA)	kA				
First stroke		101	14	30	80
Subsequent stroke		135	4.6	12	30
Charge (total charge)	C				
First stroke		93	1.1	5.2	24
Subsequent strokes		122	0.2	1.4	11
Complete flash		94	1.3	7.5	40
Impulse charge (excluding continuing current)	C				
First strokes		90	1.1	4.5	20
Subsequent strokes		117	0.22	0.95	4
Front duration (2 kA to peak)	μs				
First strokes		89	1.8	5.5	18
Subsequent strokes		118	0.22	1.1	4.5
Maximum dI/dt	kA μs^{-1}				
First strokes		92	5.5	12	32
Subsequent strokes		122	12	40	120
Stroke duration (2 kA to half peak value on the tail)	μs				
First strokes		90	30	75	200
Subsequent strokes		115	6.5	32	140
Action integral	A^2s				
First strokes		91	6.0×10^3	5.5×10^4	5.5×10^5
Subsequent strokes		88	5.5×10^2	6.0×10^3	5.2×10^4
Time interval between Strokes	ms	133	7	33	150
Flash duration	ms				
All flashes		94	0.15	13	1100
Excluding single-stroke Flashes		39	31	180	900

Table 1.1: Empirically measured lightning characteristics taken from [31].

1.2 Motivation for Study

Understanding and interpreting measured lightning emissions is necessary for accurate lightning geolocation, the measurement of a lightning strike's position in space. Lightning geolocation data is used by a diverse set of industries, ranging from forestry to aviation. Examples include utility companies which use the data for planning new power lines and fault detection in existing infrastructure; the forest industry uses the data for forest fire detection in remote areas; the energy industry uses the data to determine whether lightning may have struck an asset such as a windmill or oil derrick; the insurance industry uses the data to assess risk and verify loss claims; and air traffic controllers use the data to safely route aircraft away from hazardous lightning.

Historically, lightning location data has been provided by a few regional or national sensor networks consisting of sensor stations spread 100-200 miles apart. In the United States, a number of regional networks were consolidated into the North American Lightning Detection Network in the 1980s to save cost of what had been an infrastructure intensive undertaking which used satellite communications to coordinate sensor stations and novel precision clocks. The NALDN had been the sole provider of lightning data until the early 2000s when a second national network, the United States Precision Lightning Network, became available with comparable performance. More recently, a third network has emerged called the Earth Networks Total Lightning Network. The emergence of two new national networks in the past decade is likely due to the availability of the Internet for sensor coordination and low cost GPS clocks for sensor synchronization. In the coming decade as distributed sensor networks become more abundant to solve a vast array of problems, lightning geolocation networks should benefit as demand for relevant technology brings costs down and new technologies are developed.

Lightning locating networks measure lightning strike location using the Time of Arrival (TOA) technique which involves multiple stations measuring the time required for the electromagnetic emissions from a strike to reach a sensor, and determine the origin by comparing the arrival times across all stations. Three stations are needed to determine the origin of a lightning strike assuming the strikes are located on the Earth's surface (2D TOA). If lightning strikes that remain within a cloud are to be measured, a fourth station is required to account for the extra spatial dimension (3D TOA). 2D TOA is simpler to describe because it can be neatly diagrammed in the plane of a page and will be described in detail here; expanding the analysis to the third dimension is straightforward and is described in [3] .

When a lightning emission is detected at two spatially separated stations, the difference in arrival times corresponds with the difference in distance from each station to the signal origin. In two dimensions, the curve of constant differential distance between two points is a hyperbola with the points of interest being

the two focii of the the hyperbola. This relation is shown (1.1) and in Figure 1.1 where the distance d1-d2 is a constant equal to 2a [34]. For an emission measured by two stations, the value d is the half of the sensor baseline, a can be determined by the arrival time difference and b can be determined using (1.2).

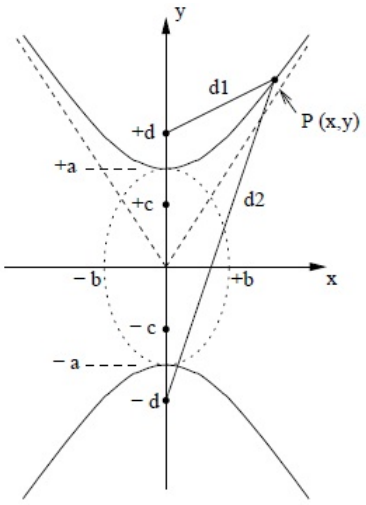

Figure 1.1: The difference of arrival time of lightning emissions at sensor stations defines a hyperbola with the sensor stations located at $\pm d$ and the sensor baseline being $2d$. Adapted from [34].

$$\frac{y^2}{a^2} - \frac{x^2}{b^2} = 1 \tag{1.1}$$

$$|d1 - d2| = 2a \tag{1.2}$$

$$a^2 + b^2 = d^2 \tag{1.3}$$

Applying this situation to 3 spatially separated stations, the time difference of a single emission can be used to draw a pair of hyperbolas, and the the intersection of the hyperbolas is the source location. This situation is demonstrated in Figure 1.2 where the bottom right station is the common focus for both hyperbolas. In this case, the strike location can be found by writing (1.1) for each sensor pair and solving the two equations for the two unknowns, x and y.

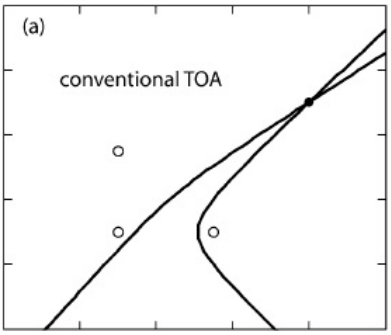

Figure 1.2: Three stations can be used to calculate two time difference hyperbolas. Above, the bottom right station is paired with the other two stations for the two hyperbolas shown. The intersection of the hyperbolas indicates the lightning strike location. Adapted from [6].

The uncertainty in the arrival time results in an uncertainty in differential distance between two stations and ultimately in strike location. In two dimensions, this results in a region of uncertainty approximately shaped like a parallelogram where the hyperbolas overlap. The uncertainty effects are exacerbated for strikes that are located outside the triangle defined by the three sensor locations. Figure 1.3 shows the broadening of the differential distance hyperbolas due to distance uncertainties and the affect on source determination for sources located inside and outside the sensor triangle or *Network*. If clock precision was the dominant source of position uncertainty, a 50 ns clock uncertainty would correspond with a c x 50 ns = 15 m side uncertainty parallelogram. The temporal resolution determined by the Time-Frequency Uncertainty Principle of Fourier Analysis can be larger than the clock uncertainty and determines the lower limit of position uncertainty regardless of clock precision; this relation is given in (1.4). Most, if not all, current operational lightning location networks operate in the VLF or LF bands, and using the LINET bandwidth of 400 kHz, for example, we find a fundamental limit on positional uncertainty of 60 m. In summary, even though current GPS technology allows for relatively inexpensive clocks with precision in the tens of nanoseconds; VLF and LF networks have a bandwidth limited temporal resolution of hundreds of nanoseconds corresponding with a spatial resolution of tens of meters.

$$\Delta f \Delta t \geq \frac{1}{4\pi} \tag{1.4}$$

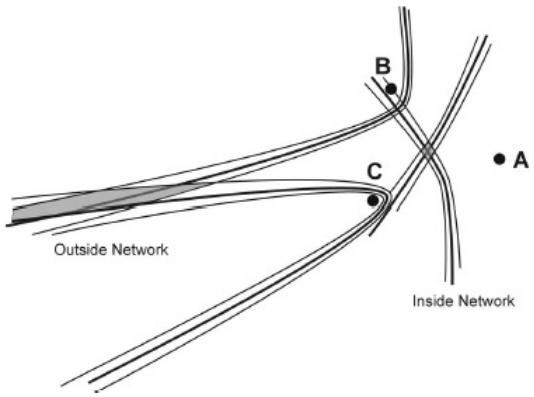

Figure 1.3: Uncertainty in the distance from the source results in a "broadening" of the hyperbolas and the region of uncertainty in source location is the parallelogram defined by the overlap of the broadened hyperbolas. For emission sources located outside of the *network* defined by the sensor locations, the uncertainty is exacerbated. Adapted from [6].

It is evident from (1.4) that it is beneficial to measure the higher frequency emissions to reduce the temporal uncertainty of the emitting process. To better understand the frequency bands which contain lightning emissions, the dominant processes resulting in emissions in the common RF frequency bands will be reviewed next. A later section serves to explain physical lightning processes in detail, but relevant qualitative descriptions will be explained as necessary. Finite ground conductivity results in a preferential attenuation of higher frequencies and must also be considered when considering frequency bands. Not only does this result in the suppression of higher frequency processes, finite ground conductivity results in the distortion of lightning waveforms in a given band, notably LF/VLF, over distance. The suppression of high frequencies is explained in detail here [42], [13], but can be explained qualitatively by the fact that the absorption coefficient in slightly lossy media is proportional to frequency. However, since the loss tangent is inversely proportional to frequency, media which are lossy at lower frequencies become low loss at high frequencies resulting in uniform attenuation above a certain thresh hold. Figure 1.4 shows frequency dependent attenuation at a number of distances in the VLF band over seawater. For example, the figure demonstrates that a 2 kHz signal will undergo ten times more attenuation than a 200 Hz signal over 50 miles, but the same frequencies undergo the same attenuation at 200 miles.

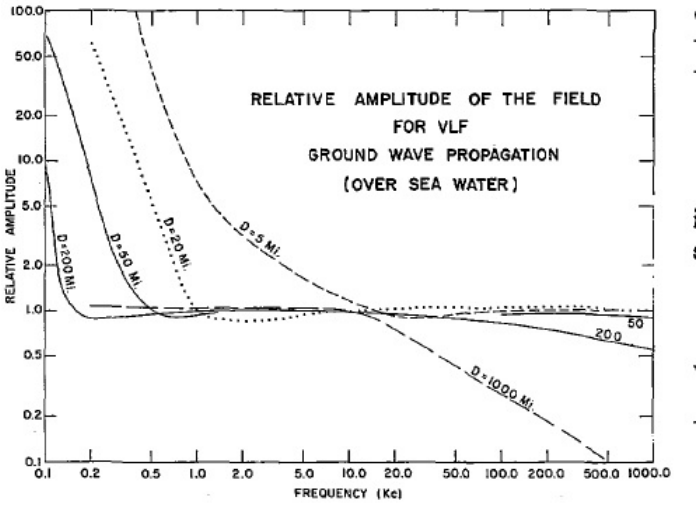

Figure 1.4: Finite conducting surfaces such as sea water or ground preferentially suppress high frequencies. Adapted from [42].

ELF emissions below 3 kHz are caused by transverse currents in the return stroke channel. The upward propagating return stroke current flows in the inner core of the lightning channel and a potential difference comparable to the pre-strike cloud to ground potential exists between the inner core and outer channel sheath. This potential difference causes lateral currents to flow in the leader channel for a duration of approximately 3 milliseconds after return stroke initiation [33]. The horizontal currents will result in horizontally polarized emissions which are orthogonal to the models and data of vertically polarized fields presented in this thesis. However, the horizontal currents are flowing through the vertical current channel and, therefore, should contribute to the vertically polarized electric emissions. These emissions are manifested as an electric field ramp seen after the impulsive emissions in lightning waveforms such as those shown in Figure 1.5.

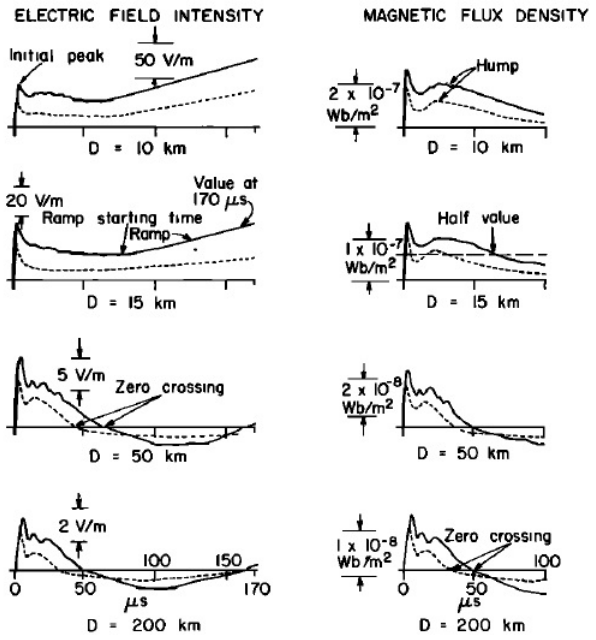

Figure 1.5: Typical lightning return stroke electric and magnetic field VLF waveforms at various distances. The solid line corresponds with the initial stroke and the dotted with subsequent strokes. Adapted from [17].

LF-VLF emissions are dominated by the upward propagating return stroke which travels at .1 to .5 c from ground to cloud neutralizing the charge left by the leader. This process is modeled in this thesis and is what is commonly measured by most lightning locating systems, and example waveforms are shown in Figure 1.5. The VLF band is advantageous for lightning detection because emissions can travel for hundreds of miles with relatively little attenuation from terrain features. Since VLF emissions are a direct result of the return stroke current, a second advantage of the band is the ability to extract the return stroke current, an important parameter for assessing potential damage, from the VLF magnetic field. The empirically confirmed modified Biot-Savart law shown in (1.5) gives the return stroke current as a function of LF/VLF magnetic field emissions; here v_{rs} is the return stroke velocity, B is the magnetic field and R is the radial distance [31].

$$I_{ReturnStroke} = \frac{2\pi RBc}{v_{rs}\mu_0} \tag{1.5}$$

MF-VHF emissions are dominated by streamer processes found during initial breakdown, the leader phase and post stroke inner-cloud processes; but not during the return stroke. Streamers, such as those found at the leader tip, have a conical shape and propagate broad-side first. The streamer cone has a dipolar charge structure with a positive tip followed by negative charge. These streamers travel at speeds near 10^5 m/s and distances up to a few km in the case of the leader. A detailed derivation of the resulting power spectrum

can be found in [26], but the properties of a typical dipole radiator can be used to bound the frequency spectrum: Streamers which propagate 100 m can be approximated by a 100 m dipole radiator with $\lambda \geq 100$ m and f $\leq$ 3 MHz. Therefore, HF and VHF emissions result from streamers which propagate relatively short distances from 1 to 100 m. The return could in principal be modeled as a large dipole streamer with a 1 km length but there would be no emissions above 300 kHz. VHF emissions are advantageous because the short wavelengths reduces the fundamental uncertainty limit to a fraction of a meter. A disadvantage of VHF systems is that they require line of site observation which would decrease the required sensor baseline, increasing sensor density, and would require sensors to be mounted to tall structures.

UHF emissions are dominated by bremsstrahlung radiation which results from electron-atom and electron-ion collisions. These collisional processes occur in both the leader and return stroke phase. However, UHF emissions are only observable in the leader because because the return stroke channel is *optically thick* in the UHF band, hence, all return stroke UHF emissions are absorbed in the channel, whereas the leader channel is optically thin resulting in the emission of UHF radiation. The difference in UHF absorption between the leader and return stroke phases is due to the degree of ionization: The leader is *partially* ionized resulting in a much smaller (by 10 orders of magnitude) absorption coefficient than the much hotter and *fully* ionized return stroke channel. Detailed review of the UHF absorption coefficient is beyond the scope of this thesis but calculations can be found here [28].

Chapter 2

Observations of Cloud Charge Structure and Lightning

In this section we review the published results of various properties of lightning and lightning producing clouds which will be used for model inputs as well as to check the plausibility of model results. Although lightning has been observed since the beginning of humanity, many basic processes such as cloud charging and lighting initiation are still not well understood and this section serves to present the current state of knowledge of the lightning strike, from cloud charging to return stroke completion.

2.1 Properties of Lightning Producing Clouds

Lightning is produced by a variety of cloud structures from the cumulonimbus cloud which makes up the classic thunderhead and anvil clouds to the extensive clouds of mesoscale cloud complexes which comprise tropical storms. Lightning can also arise from clouds of particles which are not hydrometeors such as smoke from wildfires, dust storms and volcanic ash. In this section, the physical properties of the most common lightning producing cloud, the cumulonimbus, are reviewed. Cumulonimbus clouds begin as smaller non-rain-producing cumulus clouds. As a mass of warm air rises, it does work on the surrounding environment via adiabatic expansion causing the air mass to cool. When the air mass temperature drops below the local dew point, water begins to condense on the particles forming a visible cloud. The temperature gradient with respect to altitude must be greater than or equal to the moist adiabatic lapse rate, $.6\frac{^oC}{100m}$, for adiabatic expansion of saturated air to occur; and the cloud height will continue to increase until the lapse rate falls below this rate. It should be noted that the adiabatic lapse rate for dry air is larger and a minimum gradient of 1 $\frac{^oC}{100m}$ is needed for adiabatic expansion to occur. The difference can be attributed to the latent heat released by condensation which lowers the threshold at which the air mass can do work on its environment. As the air mass rises above the 0C isotherm, it begins to freeze but the purest water droplets will supercool and remain liquid at temperatures as low as -40C. Supercooling occurs in clouds because much of the liquid

water suspended in the air mass is free of the nucleation sites necessary for ice crystals to form at the standard 0C freezing point. The stratosphere ultimately limits the height to which cumulonimbus clouds can grow because the temperature begins to increase with increasing height; this occurs at the tropopause which varies from 8km at high latitudes in the winter to 18 km in the tropics during the summer.

A typical cumulonimbus convective cell is 3 to 20 km high and 3 to 50 km wide. In general, if the relative humidity is lower at ground-level, the ground-level dew point is higher and an air mass does not need to rise as far to form a cloud; this results in humid places having lower cloud bases with respect to ground than more arid places; for example, clouds in Florida are typically lower than clouds in Colorado. A separate type of lightning producing convective cell found in large storms spanning hundreds of miles and lasting longer than a few hours is known as a Mesoscale Cloud Complex (MCC); common examples of MCCs are tropical storms and hurricanes. The charge and lightning dynamics in MCCs are distinct from that in cumulonimbus clouds and not considered in this thesis.

The classical charge structure of a cumulonimbus cloud is shown in Figure 2.1 for summer storms in Florida and New Mexico, and consists of an upper positive charge and lower negative charge with equal magnitude of approximately 25-40 C forming a dipole. Observations and theoretical models have shown and predicted additional charges at the base and top of the clouds which form a "screening" layer which will be discussed in more detail below. However, the magnitude of the additional charges are 10% of the main inner charges and are often neglected; this thesis also neglects the screening layers and treats the cloud charge structure as a simple dipole [16]. Electric field measurements of passing thunderstorms such as that shown in Figure 2.2, as well as in situ measurements using balloons, confirm the validity of the dipole model [14] , [12]. This data has the expected features of an upward oriented dipole above a grounded plane with an upward directed field near cloud center where the lower charge dominates and a downward directed field at large distances due to the positive charge entering the observer's field of view.

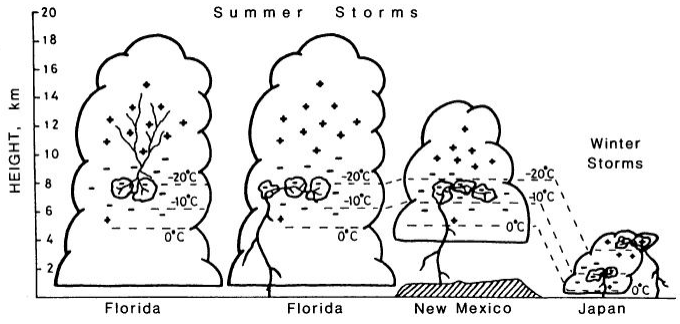

Figure 2.1: The typical cloud structure found in summer time cumulonimbus clouds. Notice that the charge location are roughly independent of the height above ground and are instead a strong function of isotherm. Adapted from [16].

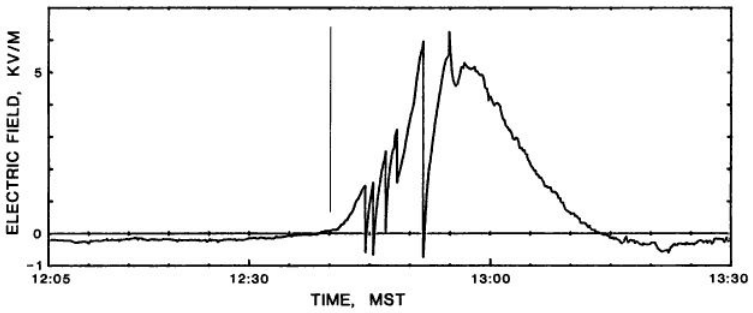

Figure 2.2: Cloud charge measurements made from ground of a thunderstorm passing approximately 5km from a fixed observation point; an upward-directed electric field is defined as positive. The overall field shape is consistent with that of a dipole cloud charge. The sharp, transient decrease is electric field is due to charge removal from lightning strikes. Adapted from [16].

Any cloud charging model must explain the predominant dipole structure observed in nature and provide a small-scale mechanism for cloud formation. The currently favored theory attributes the cloud structure formation to non-inductive particle charging and is commonly referred to as the *Graupel Ice Mechanism* [32]. Graupel is soft ice formed high in a cloud which falls downward due to gravity through a medium of lighter suspended ice crystals which results in constant collisions of the graupel with the crystals making up the surrounding medium. Depending on the ambient temperature where the collisions occur, the graupel will either lose electrons to the medium or gain electrons from the medium; laboratory experiments have shown the presence of supercooled water enhances the charge transfer. The temperature at which the graupel switches charge polarity is known as the *Reversal Temperature* and occurs between -20 and -10 C. The charge transfer mechanism is believed to be related to the physics at the ice surface but there is no consensus as to the cause. One theory proposed in [2] suggests that ice is covered with a surface layer of OH^- ions and it is believed that the particle with the faster growing ice surface gains a positive charge from a collision because it leaves some of its OH^- with the other particle. High in the cloud, the suspended ice crystals are growing faster than the passing graupel; but at lower warmer altitudes, the graupel begins growing at a relatively faster rate. Applying this to the cloud environment, the falling graupel becomes negatively charged in the colder and higher regions of the cloud leaving the upper cloud with a positive charge. As the graupel passes the -20C isotherm, it begins to lose its negative charge to the surrounding medium leaving the lower cloud with a negative charge and the resulting structure is shown in Figure 2.1.

Another cloud charging mechanism, which had been the leading mechanism historically, is the *Convection Mechanism*. It has fallen out of favor recently as experimental verification of the mechanism has proven inconclusive and numerical modeling has shown the mechanism insufficient to account for the total cloud charge [37], [23], [35]. It is nevertheless reviewed here because even if it is not the dominant mechanism

for cloud charging; it is still a plausible mechanism for charge transport within a cloud and may play a roll in the reconstruction of the cloud dipole after a lightning discharge which happens at fast timescales as is shown in the data in Figure 2.2. The convection mechanism is shown graphically in Figure 2.3. In the convection mechanism, electric charge is supplied by external forces, namely corona and fair-weather space charge caused by radioactive decay of isotopes in the ground and ionization due to cosmic rays near the cloud top. Convection then causes the charge separation: Warm air currents known as up-drafts carry positive charge near the ground towards the top of the cloud. Negative charge produced by cosmic rays above the cloud is then attracted to the cloud boundary by the positive charge within. Down-drafts along the outer cloud boundary transfer the negative charge downward to the cloud bottom. The negative charge at the cloud bottom causes corona at the surface and hence positive feedback for the process.

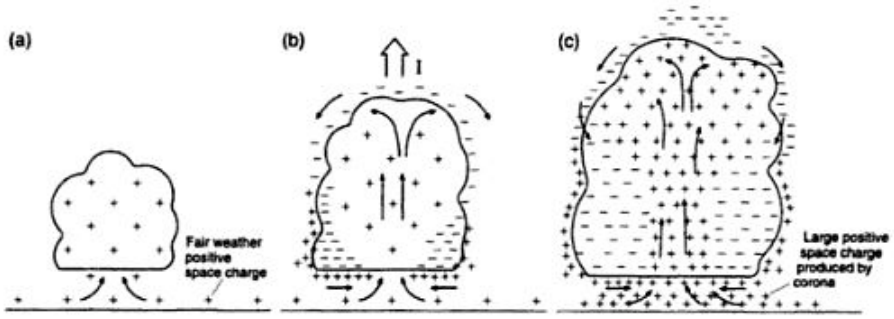

Figure 2.3: a. Warm air currents known as up-drafts carry positive charge near the ground towards the top of the cloud. b. Negative charge produced by cosmic rays above the cloud is then attracted to the cloud boundary by the positive charge within. c. Down-drafts along the outer cloud boundary transfer the negative charge downward to the cloud bottom. The negative charge at the cloud bottom causes corona at the surface and hence positive feedback for the process. Adapted from [18].

Next we will review how charge is physically organized within a cumulonimbus cloud. Observational evidence suggests that cloud charge is organized as discrete charge centers which are horizontally displaced within the cloud with the charge polarity being a strict function of temperature and height and having a charge density of 20 C/km^3 [43]. Krehbiel studied the inner cloud charge processes in detail through ground measurements made in conjunction with radar measurements which give insight into how charge is organized and transported within a cloud during a lightning flash [15]. Figure 2.4 is an example of these measurements which show the relative charge magnitude and location for the multiple strokes making up a single lightning flash. These data assume a spherical charge center with a 20 C/km^3 charge density and can be analyzed as follows. Considering the example of Flash 17, the spheres represent the charge centers and the adjacent numbers indicate the stroke order. Stroke 1 lowered the largest charge center to ground and the approximate horizontal displacement of the successive charge centers is 1 km. It is important to note that the vertical

lines do not represent the leader/return stroke position at ground, rather they are to make it easier to view the x-y location of the cloud charge centers. Because most strokes in a single flash follow the trajectory of the initial stepped leader (stroke 1), it is assumed that although the cloud charge centers are displaced by as much as 5 km; they all share the same trajectory to ground beneath the cloud base.

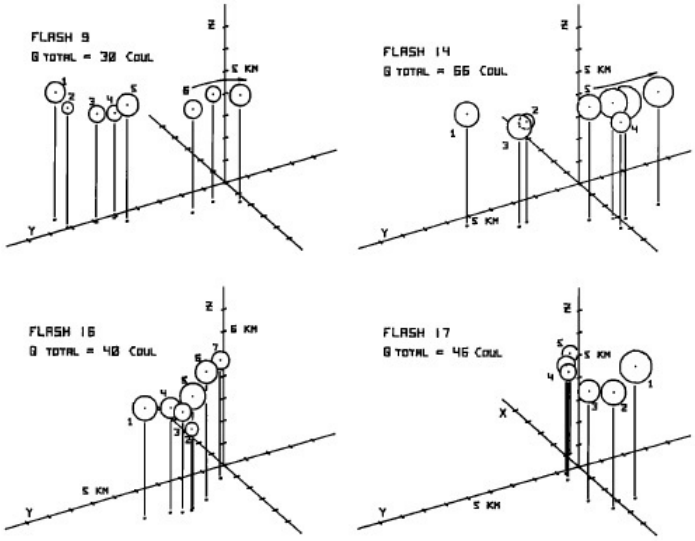

Figure 2.4: Cloud charge position measurements. The z axis indicates the height above ground and the x and y axis indicate horizontal displacement. The circles indicate relative spherical charge size, and the adjacent numbers indicate stroke order. Adapted from [15].

Balloon soundings taking in-situ electric field measurements of a number of lightning producing clouds were analyzed in [21]. The authors integrated the electric field with respect to ground and found the inner cloud voltages to vary from -102 to 94 MV; a sample profile is shown in Figure 2.5 and was chosen because the negative and positive charge heights of approximately 6 and 9 km, respectively, are in close agreement with the average values of 7 and 12 km used in the model developed here. Note that the charge locations can be determined from the figure by applying Gauss's Law in one dimension; the sign convention is such that a positive slope in the figure corresponds with positive charge. It should be noted that although balloon measurements provide the ability to measure the local electric field as a function of height, hence providing a profile of the cloud characteristics; they are inherently slow taking 20-40 minutes to traverse a storm during which the charge structure is evolving. Furthermore, the path a balloon takes is determined by local convection and it is unlikely the balloon will pass the areas of largest charge concentration.

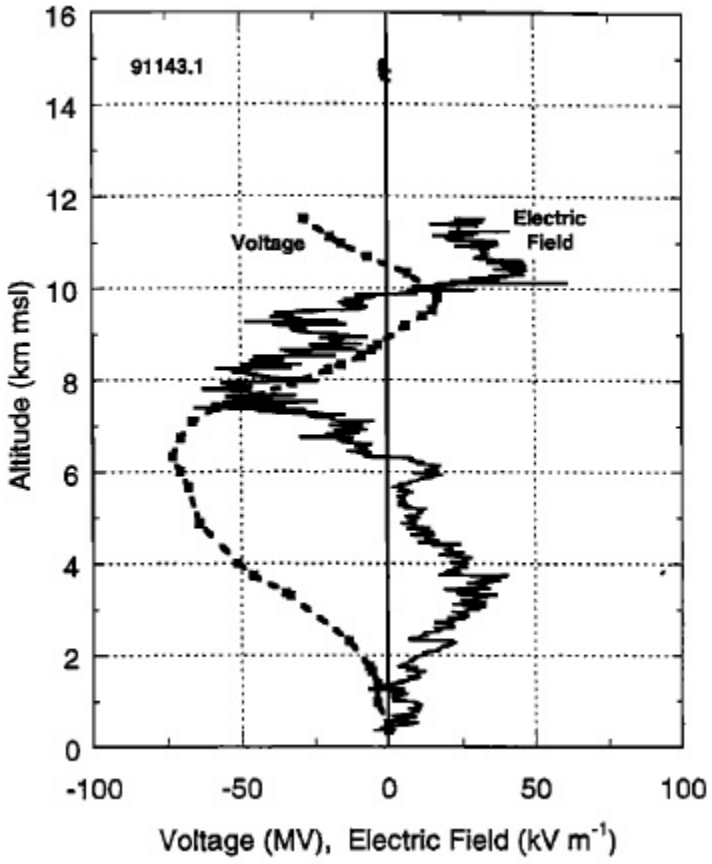

Figure 2.5: An example cloud electric field and voltage profile taken from [21].

2.2 Properties of the Lightning Leader

What is commonly observed as a cloud-to-ground lightning flash consists of one or more lightning strikes. The lightning leader is the first step in the 3 distinct phases of a lightning strike; the second and third steps being attachment and the return stroke. The first strike in any lightning flash is unique because it takes place in undisturbed air and exhibits a stepped or halting behavior as the charge seeks out the most direct path to ground. The subsequent strikes typically proceed in a smooth fashion because they follow the hot, thermally ionized and, hence, conductive column of air produced by the preceding strike(s). Table 2.1 shows the temperature, resistance, radius and conductivity of the lightning channel or air column at various stages in the lightning flash; notice that the channel left by a previous strike preceding a dart leader has a conductivity of .02 Sm^{-1} which far exceeds the conductivity of air which is 10^{-14} Sm^{-1} at sea level [32]. This thesis focuses exclusively on the dart leader and subsequent return stroke; therefore, the stepped leader, initial return stroke and attachment process will not be discussed in detail

Channel Characteristics	Pre-dart-leader channel (ahead of dart-leader front)	Pre-return-stroke channel (behind dart-leader front and ahead of return stroke front)	Return-stroke channel (behind return-stroke front)
Temperature, K	∼3,000	≥20,000	≥30,000
Conductivity, S m^{-1}	∼0.02	$\sim 10^4$	$\sim 10^4$
Radius, cm	∼ 3	∼0.3	∼3
R, Ω m^{-1}	∼18,000	∼3.5	∼0.035

Table 2.1: Typical lightning channel characteristics. Adapted from [32].

The lightning initiation process is not well understood; nevertheless one hypothesis is presented here as an example. The maximum electric fields generated by the large scale cloud charge distributions are below the breakdown field of 1 x 10^6 Vm^{-1} needed in the cloud environment. Note, the breakdown field for dry air at sea level is 3 times larger than it is within a cloud; the difference being due to reduced air pressure and the presence water droplets [20]. Hydrometeors undergo significant deformation in the presence of the intense fields within a cloud causing the emission of positive corona streamers; the streamers are postulated to be positive because positive streamers can propagate in lower fields; the threshold for propagation being 1.5 x 10^5 Vm^{-1} at which point the ionization probability exceeds the attachment probability in an electron collision with an air molecule. If a series of tenuous streamers develop in the same vicinity; the electric field can be enhanced sufficiently to exceed the breakdown threshold over a distance of a few meters. Laboratory experiments and modeling of discharges across widely spaced plates of 10 m or more give insight into how and why a lightning leader propagates from cloud to ground [7].

Once the breakdown field is exceeded, a stable streamer can form. The streamer tip consists highly concentrated positive ions and excited molecules. Spontaneously emitted photons from the excited molecules can photo-ionize nearby air molecules which can ionize additional molecules through collisions with the photo-ionized electrons. The net result is a self-sustaining avalanche process which advances the streamer tip through ionization of nearby air molecules. The streamer can propagate in fields below the breakdown field as long as its *built-in* field exceeds the breakdown field. Many such streamers compose the leader tip which leaves behind a conductive weakly ionized channel into which the cloud charge flows. The total charge in a typical leader is 1 C; and the average leader current is 1 kA. Typical values for the dart leader velocity are 1-2 x 10^7 m/s [32] and recent measurements have shown the velocity to be constant [19]; although

earlier measurements have shown both acceleration or deceleration near ground. One explanation for the discrepancy may be that earlier measurements were taken with streak photography which is inherently two dimensional and unable to detect tortuosity in the unmeasured spatial dimension.

2.3 Properties of the Lightning Return Stroke

As the leader approaches ground, the intense local electric field induce corona followed by upward streamers at ground level which intercept the leader tens of meters above ground initiating the return stroke at attachment. The return stroke serves to neutralize the charge in the leader column and its transient nature and extreme environment have made direct measurements of natural return strokes difficult. Rocket induced lightning has also been studied but comparisons of remote measurements of rocket induced and natural lightning show them to have distinct characteristics. Nevertheless, the naturally occurring return stroke has been the most studied component via instrumented towers and remote sensing. The subsequent return stroke following a dart leader typically has a peak current of 10-15 kA which transfers the 1 C leader charge to ground. This intense current heats the air column to 30,000 K, more than 5 times hotter than the surface of the sun, leaving behind a neutral but hot and conductive air column for which additional leaders can travel lowering additional nearby charge concentrations to ground.

The return stroke velocity has been historically measured using streak photography and the most extensive published data-sets have been measured with this technique [4], [11]; another method in the literature measures the optical pulse a various heights along the return stroke channel extrapolates the velocity from the return stroke optical pulse arrival time as a function of height. The earliest measurements suggested that the subsequent return stroke had a constant velocity; but the initial return stroke had a velocity which varied exponentially in time [36].

The initial return stroke is typically modeled using a double exponential of the form shown in (2.1) first developed in [38] which is fit to empirical data at larger times as the velocity is decreasing; and is constrained to having zero initial velocity and to not exceed the speed of light. An extensive search of the literature did not reveal any published *empirical* velocity models specifically for subsequent return strokes; and this was not modeled in [38] because the subsequent return stroke velocity was believed to be constant at the time. However, more recent measurements have shown the subsequent return stroke to vary sharply with height near the surface; and it is postulated earlier measurements missed this trend because they observed higher portions of the leader column. Nevertheless, the more later subsequent return stroke results were not found to be formulated and published as a mathematical model.

$$v(t) = V_o(e^{-at} - e^{-bt}) \tag{2.1}$$

It should be noted that there are numerous published subsequent return stroke models, some of which will be reviewed in Section 4.3. Most of these models depend on velocity, but rather than using direct velocity observations as an input; they invert the process and use the general form of (2.1) and determine the model parameters by how the modeled return stroke electromagnetic waveforms agree with observation [8]. Cooray developed a model in [5] which predicts the return stroke velocity as function of height based on the channel charge time evolution and it is shown in Figure 5. Since this thesis attempts to model the dart leader and subsequent return stroke electromagnetic fields from first principles independently, the velocity model was chosen to be empirically based rather than rely on a published velocity model which is dependent on a specific electromagnetic field model.

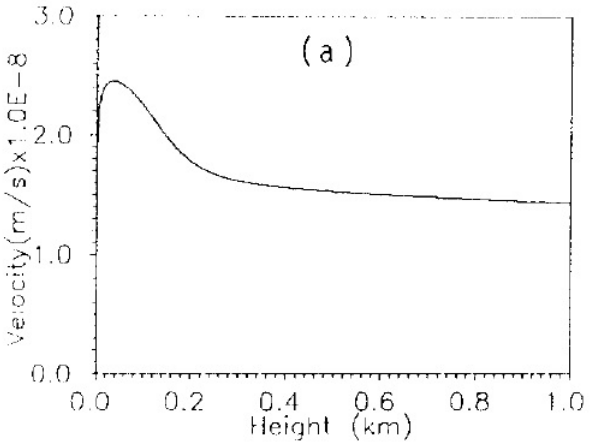

Figure 2.6: Results for velocity from a electromagnetic model of a subsequent return stroke. Adapted from [5]

In lieu of a published subsequent return stroke model; an original model is developed which meets the following conditions: 1) The model follows the the form of (2.1) proposed by [38], 2) the model approaches a constant velocity at large heights and times, and 3) the model agrees with observation. This resulting model is shown in (5) and plotted in Figure 2.7 along with the original model developed in [38] and data taken from [11]. A notable flaw in this model is the non-zero start velocity. Regarding the higher peak velocity of the modified srivastava model when compared to the original, published observations in [11] showed subsequent return strokes to be faster, on average, than the initial return stroke; a physical explanation for this is the subsequent dart leader channels lack the branching evident in initial stepped leaders providing the subsequent return stroke a more direct return path to the cloud.

$$v(t) = 2.9006 \times 10^8 (e^{-3.1245\times10^5 s^{-1} t} - e^{-7.9316\times10^6 s^{-1} t}) \frac{m}{s} + 5 \times 10^7 \frac{m}{s} \tag{2.2}$$

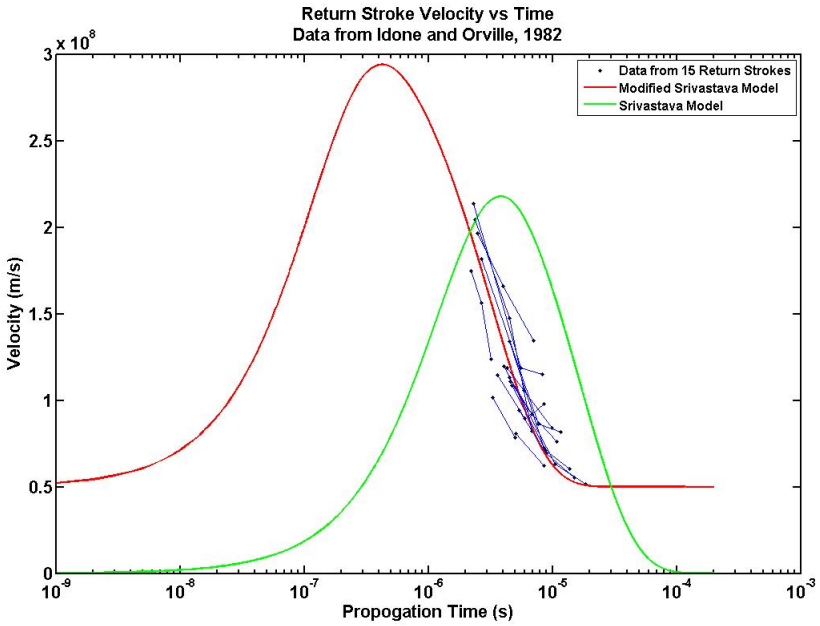

Figure 2.7: The original double exponential velocity model developed by Srivastava for the initial return stroke [38] is compared with subsequent return stroke velocity measurement data [11] and the Modified Srivastava Model used in this Thesis. Individual return strokes are distinguished by lines connecting the velocity measurements.

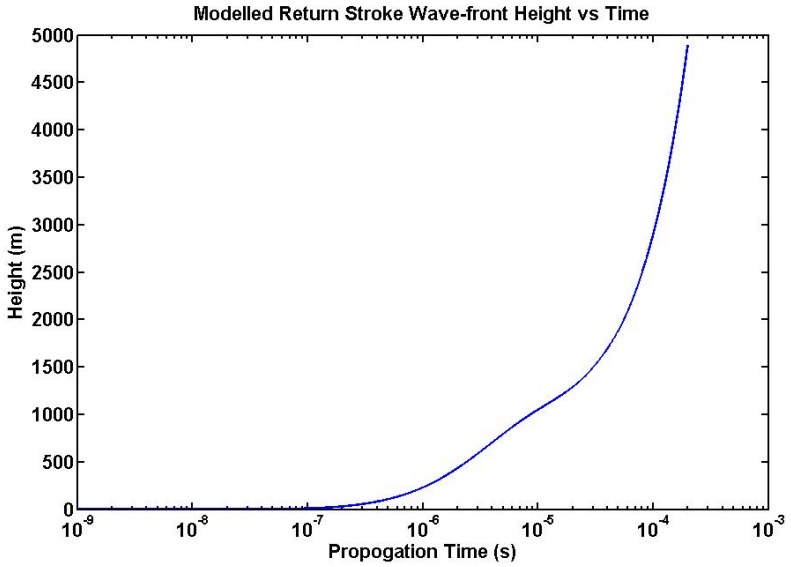

Figure 2.8: The return stroke height as a function of time given by (5).

Chapter 3

Mathematical Development of the Leader Fields

In this section we will develop a model for the leader electromagnetic fields based on the leader charge and current. First, we derive the general expression for the electric and magnetic fields of an arbitrary charge and current distribution starting with Maxwell's Equations.

3.1 Leader Electric and Magnetic Fields from First Principles

Maxwell's Equations:

$$\text{Gauss's Law: } \vec{\nabla} \cdot \vec{E} = \frac{1}{\epsilon_o}\rho \tag{3.1}$$

$$\text{No Magnetic Monopole: } \vec{\nabla} \cdot \vec{B} = 0 \tag{3.2}$$

$$\text{Faraday's Law: } \vec{\nabla} \times \vec{E} = -\frac{\partial \vec{B}}{\partial t} \tag{3.3}$$

$$\text{Ampere's Law: } \vec{\nabla} \times \vec{B} = \mu_o \vec{J} + \mu_o \epsilon_o \frac{\partial \vec{E}}{\partial t} \tag{3.4}$$

Following the standard process, we define mathematical constructs commonly known as the vector and scalar potentials which we require to be consistent with Maxwell's Equations. Since the magnetic field is divergence-less according to (3.2), we can define the Vector Potential, $\vec{A}$, as the curl of the magnetic field.

$$\vec{B} = \vec{\nabla} \times \vec{A} \tag{3.5}$$

Putting (3.5) into Faraday's Law, (3.3), yields

$$\vec{\nabla} \times \vec{E} = -\frac{\partial}{\partial t}(\vec{\nabla} \times \vec{A})$$

$$\vec{\nabla} \times \left(\vec{E} + \frac{\partial \vec{A}}{\partial t} \right) = 0 \tag{3.6}$$

Since the curl of a gradient is zero, we can define the quantity in (3.6) in parenthesis to be the gradient of the scalar potential.

$$\vec{E} = -\vec{\nabla}\phi - \frac{\partial \vec{A}}{\partial t} \tag{3.7}$$

(3.5) and (3.7) give us expressions for the magnetic and electric fields in terms of the scalar and vector potentials. Our next task is to find the scalar and vector potentials in terms of the source current and charge distributions.

Putting (3.7) into Gauss's Law, (3.1), yields

$$\nabla^2 \phi + \frac{\partial}{\partial t}(\vec{\nabla} \cdot \vec{A}) = -\frac{1}{\epsilon_o}\rho \tag{3.8}$$

Putting (3.5) and (3.7) into Ampere's Law, (3.4) yields

$$\vec{\nabla} \times (\vec{\nabla} \times \vec{A}) = \mu_o \vec{J} - \mu_o \epsilon_o \nabla \left(\frac{\partial \phi}{\partial t} \right) - \mu_o \epsilon_o \frac{\partial^2 \vec{A}}{\partial t^2}$$

Using the vector ID: $\vec{\nabla} \times (\vec{\nabla} \times \vec{A}) = \nabla(\nabla \cdot \vec{A}) - \nabla^2 \vec{A}$

$$\left(\nabla^2 \vec{A} - \mu_o \epsilon_o \frac{\partial^2 \vec{A}}{\partial t^2} \right) - \nabla \left(\nabla \cdot \vec{A} + \mu_o \epsilon_o \frac{\partial \phi}{\partial t} \right) = -\mu_o \vec{J} \tag{3.9}$$

We have the freedom to impose further restrictions on our mathematical construct, $\vec{A}$, as long as they are consistent with Maxwell's Equations, and can choose the divergence of $\vec{A}$ to be any quantity without affecting the $\vec{E}$ or $\vec{B}$ fields. Choosing the Lorentz Gauge, $\nabla \cdot \vec{A} = -\mu_o \epsilon_o \frac{\partial \phi}{\partial t}$, eliminates middle term in (3.9). And (3.8) and (3.9) can now be written in similar form:

$$\nabla^2 \vec{A} - \mu_o \epsilon_o \frac{\partial^2 \vec{A}}{\partial t^2} = -\mu_o \vec{J} \tag{3.10}$$

$$\nabla^2\phi - \mu_o\epsilon_o\frac{\partial^2\phi}{\partial t^2} = -\frac{1}{\epsilon_o}\rho \tag{3.11}$$

with general solutions of the form:

$$\phi(\vec{r},t) = \frac{1}{4\pi\epsilon_o}\int\frac{\rho(\vec{r}',t_r)}{s}d\tau' \tag{3.12}$$

$$\vec{A}(\vec{r},t) = \frac{\mu_o}{4\pi}\int\frac{\vec{J}(\vec{r}',t_r)}{s}d\tau' \tag{3.13}$$

Here, τ' is always taken over the entire source unless explicitly stated otherwise, and s is the separation between the source (primed coordinate system) and observer (unprimed coordinate system); see (3.15) below. In (3.12) and (3.13), t_r is the delayed time. This is the time it takes for information traveling at the speed of light to travel from the source to an observer located a distance, s, away.

$$t_r = t - \frac{s}{c} \tag{3.14}$$

$$\vec{s} = \vec{r} - \vec{r}' \tag{3.15}$$

(3.13) and (3.12) can be inserted into (3.5) and (3.7) to derive analytic solutions for the electric and magnetic fields directly from the charge sources. However, in practice the resulting integrals are more difficult to solve than taking derivatives of the vector and scalar potentials. For completeness, this derivation is presented next, but (3.13), (3.12), (3.5) and (3.7) will be used to solve the leader electromagnetic fields.

We begin by seeking the terms in (3.7), starting by taking the gradient of the right hand side of (3.12).

$$\nabla\phi = \frac{1}{4\pi\epsilon_o}\int\left[(\nabla\rho)\frac{1}{s} + \rho\nabla\left(\frac{1}{s}\right)\right]d\tau' \tag{3.16}$$

$$\nabla\phi = \frac{1}{4\pi\epsilon_o}\int[-\frac{1}{c}\frac{\partial\rho}{\partial t}\frac{\hat{s}}{s} - \rho\frac{\hat{s}}{s^2}]d\tau' \tag{3.17}$$

Next, we take the time derivative of (3.35) to find the second term in (3.7).

$$\frac{\partial \vec{A}}{\partial t} = \frac{\mu_o}{4\pi} \int \frac{\partial \vec{J}(\vec{r}', t_r)}{\partial t} \frac{1}{s} d\tau' \tag{3.18}$$

Using equations (3.17) and (3.18) to solve equation (3.8), we find:

$$\vec{E}(\vec{r}, t) = -\frac{1}{4\pi\epsilon_o} \int [-\frac{1}{c}\frac{\partial \rho}{\partial t}\frac{\hat{s}}{s} - \rho\frac{\hat{s}}{s^2}] d\tau' - \frac{\mu_o}{4\pi} \int \frac{\partial \vec{J}(\vec{r}', t_r)}{\partial t} \frac{1}{s} d\tau' \tag{3.19}$$

Next, we find an explicit expression for the B field using (3.35):

$$\begin{aligned} \vec{B} &= \nabla \times \vec{A} \\ &= \frac{\mu_o}{4\pi} \int \nabla \times \left(\frac{\vec{J}(\vec{r}', t_r)}{s} \right) d\tau' \\ &= \frac{\mu_o}{4\pi} \int \left[\frac{1}{s}(\nabla \times \vec{J}) - \vec{J} \times \nabla \left(\frac{1}{s} \right) \right] d\tau' \end{aligned}$$

Change of variables: $(\nabla \times \vec{J})_x = -\frac{1}{c}\left(\frac{\partial J_z}{\partial t}\frac{\partial s(t_r)}{\partial y} - \frac{\partial J_y}{\partial t}\frac{\partial s(t_r)}{\partial z} \right) = \frac{1}{c}\left[\frac{\partial \vec{J}}{\partial t} \times (\nabla s) \right]_x$

$$\vec{B}(\vec{r}, t) = \frac{\mu_o}{4\pi} \int \left[\frac{\vec{J}(\vec{r}', t_r)}{s^2} + \frac{\frac{\partial \vec{J}(\vec{r}, t_r)}{\partial t}}{cs} \right] \times \hat{s} d\tau' \tag{3.20}$$

3.2 Leader Charge and Current Distribution

The leader is defined in Figure 3.1 as a propagating uniform current pulse originating from a negative point charge; the point charge, Q_C^- , represents the lower charge distribution in a typical thundercloud and Q_C^- represents the positive charge. This model considers the more common downward negative lightning flash, therefore the charge distribution in the leader will have a net negative charge.

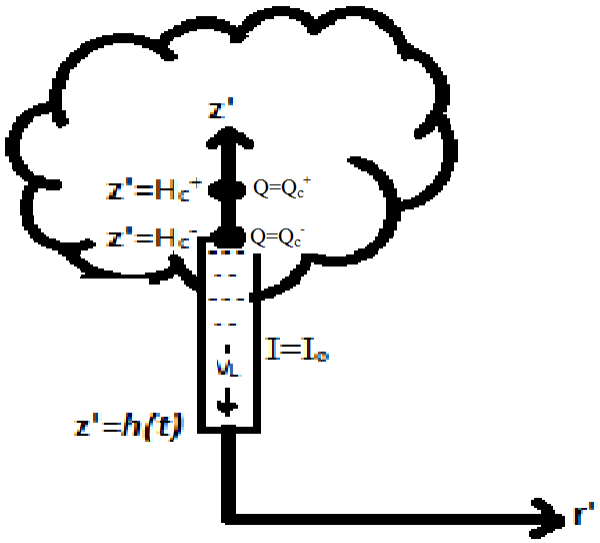

Figure 3.1: Leader source current and charge distribution.

The leader current as a function of height and time can be written in cylindrical coordinates as:

$$\vec{J}(r', \phi', z', t) = I_o \delta^2(r') \left[u(z' - h(t)) - u(z' - H_c^-)\right] \hat{z} \tag{3.21}$$

where $h(t) = H_c^- - v_L t$.

We can find the charge distribution directly from the continuity equation for charge conservation which has the added benefit of ensuring our charge and current distributions are self-consistent.

$$\text{The Continuity Equation:} \quad -\frac{\partial \rho}{\partial t} = \vec{\nabla} \cdot \vec{J} \tag{3.22}$$

Plugging (3.21) into (3.22) yields:

$$\begin{aligned} -\frac{\partial \rho}{\partial t} &= \vec{\nabla} \cdot \left(I_o \delta^2(r') \left[u(z' - h(t)) - u(z' - H_c^-)\right] \hat{z}\right) \\ \frac{\partial \rho}{\partial t} &= -I_o \delta^2(r') \left[\delta(z' - h(t)) - \delta(z' - H_c^-)\right] \end{aligned}$$

Next, integrating both sides with respect to time.

$$\int_0^t \frac{\partial \rho}{\partial t} dt = -I_o \delta^2(r') \int_{0^+}^t \delta(z' - H_c^- + v_L t) - \delta(z' - H_c^-) dt + \rho(t=0)$$

$$\rho(\vec{r'}, t) = -\frac{I_o}{v_L} \delta^2(r') \left[u(z' - h(t)) - u(z' - H_c^-) \right] + I_o u(t) t \delta(z' - H_c^-) \delta^2(r') + \rho(t=0)$$

$$\rho(\vec{r'}, t) = \frac{-I_o}{v_L} \left[(u(z' - h(t)) - u(z' - H_c^-)) + (I_o u(t) t + Q_c^-) \delta(z' - H_c^-) + Q_c^+ \delta(z' - H_c^+) \right] \delta^2(r') \tag{3.23}$$

Summarizing, the leader current consists of negative charge moving in the negative $\hat{z}$ direction and is, therefore, a positive quantity. The charge density consists of a uniform charge distribution, $-\frac{I_o}{v_L}$, with the same shape as the current distribution.

Leader Current Distribution:

$$\vec{J}(r', \phi', z', t) = I_o \delta^2(r') \left[u(z' - h(t)) - u(z' - H_c^-) \right] \hat{z}$$

Leader Charge Distribution:

$$\begin{aligned} \rho(\vec{r}, t) = &-\frac{I_o}{v_L} \delta^2(r') \left[u(z' - h(t)) - u(z' - H_c^-) \right] \\ &+ ((I_o u(t) t + Q_c^-) \delta(z' - H_c^-) + Q_c^+ \delta(z' - H_c^+)) \delta^2(r') \end{aligned}$$

3.3 Isolated Leader Fields

Although the leader fields are significantly influenced by the grounded earth, we will first consider the less complex configuration of the leader fields in the absence of any other conductors. We start by calculating

the retarded scalar and vector potentials by plugging (3.21) and (3.23) into (3.12) and (3.13)

$$\begin{aligned}\phi(\vec{r},t) = &-\frac{I_o}{v_L}\frac{1}{4\pi\epsilon_o}\int\int\delta^2(r')r'dr'd\phi'\int_{h(t_r)}^{H_c^-}\frac{[u(z'-h(t_r))-u(z'-H_c^-)]}{\sqrt{r^2+(z-z')^2}}dz' \\ &+\frac{1}{4\pi\epsilon_o}\int_{h(t_r)}^{H_c^-}\frac{I_o\left(t-\frac{\sqrt{r^2+(z-z')^2}}{c}\right)u\left(t-\frac{\sqrt{r^2+(z-z')^2}}{c}\right)+Q_c^-}{\sqrt{r^2+(z-z')^2}}\delta(z'-H_c^-)dz'\int\int\delta^2(r')r'dr'd\phi' \\ &+\frac{1}{4\pi\epsilon_o}\int_{h(t_r)}^{H_c^+}\frac{Q_c^+}{\sqrt{r^2+(z-z')^2}}\delta(z'-H_c^+)dz'\int\int\delta^2(r')r'dr'd\phi'\end{aligned} \tag{3.24}$$

$$\begin{aligned}\phi(\vec{r},t) = &-\frac{I_o}{v_L}\frac{1}{4\pi\epsilon_o}\int_{h(t_r)}^{H_c^-}\frac{[1-0]}{\sqrt{r^2+(z-z')^2}}dz' \\ &+\frac{1}{4\pi\epsilon_o}\int_{h(t_r)}^{H_c^-}\frac{I_o\left(t-\frac{\sqrt{r^2+(z-z')^2}}{c}\right)u\left(t-\frac{\sqrt{r^2+(z-z')^2}}{c}\right)+Q_c^-}{\sqrt{r^2+(z-z')^2}}\delta(z'-H_c^-)dz' \\ &+\frac{1}{4\pi\epsilon_o}\int_{h(t_r)}^{H_c^+}\frac{Q_c^+}{\sqrt{r^2+(z-z')^2}}\delta(z'-H_c^+)dz'\end{aligned} \tag{3.25}$$

$$\begin{aligned}\phi(\vec{r},t) = &-\frac{I_o}{v_L}\frac{1}{4\pi\epsilon_o}\ln\left|\frac{H-z+\sqrt{r^2+(H-z)^2}}{h(t_r)-z+\sqrt{r^2+(h(t_r)-z)^2}}\right|+\frac{1}{4\pi\epsilon_o}\frac{Q_c^+}{\sqrt{r^2+(z-H_c^+)^2}} \\ &+\frac{1}{4\pi\epsilon_o}\left(\frac{I_o\left(t-\frac{\sqrt{r^2+(z-H_c^-)^2}}{c}\right)u\left(t-\frac{\sqrt{r^2+(z-H_c^-)^2}}{c}\right)+Q_c^-}{\sqrt{r^2+(z-H_c^-)^2}}\right)\end{aligned} \tag{3.26}$$

where we used $\int\frac{du}{\sqrt{u^2+a^2}} = \ln\left|u+\sqrt{u^2+a^2}\right|+C$

Now, finding the Vector Potential.

$$\begin{aligned}\vec{A}(\vec{r},t) &= \frac{I_o\mu_o}{4\pi}\int_{h(t_r)}^{H_c^-}\frac{[u(z'-h(t_r))-u(z'-H_c^-)]}{\sqrt{r^2+(z-z')^2}}\hat{z}dz'\int\int\delta^2(r')r'dr'd\phi' \\ &= \frac{I_o\mu_o}{4\pi}\int_{h(t_r)}^{H_c^-}\frac{[1-0]}{\sqrt{r^2+(z-z')^2}}\hat{z}dz'\end{aligned}$$

$$\vec{A}(\vec{r},t) = \frac{I_o\mu_o}{4\pi}\ln\left|\frac{H-z+\sqrt{r^2+(H-z)^2}}{h(t_r)-z+\sqrt{r^2+(h(t_r)-z)^2}}\right|\hat{z} \tag{3.27}$$

Next, we solve for the gradient of the scalar potential component-wise.
For clarity, we make the substitution $u_H(t_r) = u\left(t-\frac{\sqrt{r^2+(z-H_c^-)^2}}{c}\right)$

note: there is a scalar potential ϕ and a coordinate ϕ in the next two equations.

$$\vec{\nabla}\phi = \frac{\partial\phi}{\partial r}\hat{r} + \frac{1}{r}\frac{\partial\phi}{\partial\phi}\hat{\phi} + \frac{\partial\phi}{\partial z}\hat{z}$$

$$\frac{1}{r}\frac{\partial\phi}{\partial\phi}\hat{\phi} = 0$$

$$\vec{\nabla}\phi = \frac{\partial\phi}{\partial r}\hat{r} + \frac{\partial\phi}{\partial z}\hat{z}$$

$$\begin{aligned}\frac{\partial\phi}{\partial r}\hat{r} = &-\frac{I_o}{v_L}\frac{1}{4\pi\epsilon_o}\frac{1}{H_c^- - z + \sqrt{r^2 + (H_c^- - z)^2}}\cdot\frac{r}{\sqrt{r^2 + (H_c^- - z)^2}}\hat{r} \\ &+ \frac{I_o}{v_L}\frac{1}{4\pi\epsilon_o}\frac{1}{h(t_r) - z + \sqrt{r^2 + (h(t_r) - z)^2}}\cdot\left(\frac{\partial h(t_r)}{\partial r} + \frac{r + \frac{\partial h(t_r)}{\partial r}(h(t_r) - z)}{\sqrt{r^2 + (h(t_r) - z)^2}}\right)\hat{r} \\ &- \frac{r}{4\pi\epsilon_o}\left(\frac{I_o\left(t - \frac{\sqrt{r^2 + (z - H_c^-)^2}}{c}\right)u_H(t_r) + Q_c^-}{(r^2 + (H_c^- - z)^2)^{\frac{3}{2}}} + \frac{Q_c^+}{(r^2 + (H_c^+ - z)^2)^{\frac{3}{2}}} + \frac{I_o u_H(t_r)}{c(r^2 + (z - H_c^-)^2)}\right)\hat{r}\end{aligned} \tag{3.28}$$

$$\begin{aligned}\frac{\partial\phi}{\partial z}\hat{z} = &-\frac{I_o}{v_L}\frac{1}{4\pi\epsilon_o}\frac{1}{H_c^- - z + \sqrt{r^2 + (H_c^- - z)^2}}\cdot\left(-1 + \frac{z - H_c^-}{\sqrt{r^2 + (H_c^- - z)^2}}\right)\hat{z} \\ &+ \frac{I_o}{v_L}\frac{1}{4\pi\epsilon_o}\frac{1}{h(t_r) - z + \sqrt{r^2 + (h(t_r) - z)^2}}\cdot\left(\frac{\partial h(t_r)}{\partial z} - 1 + \frac{(z - h(t_r))\left(1 - \frac{\partial h(t_r)}{\partial z}\right)}{\sqrt{r^2 + (h(t_r) - z)^2}}\right)\hat{z} \\ &- \frac{z - H_c^-}{4\pi\epsilon_o}\left(\frac{I_o\left(t - \frac{\sqrt{r^2 + (z - H_c^-)^2}}{c}\right)u_H(t_r) + Q_c^-}{(r^2 + (H_c^- - z)^2)^{\frac{3}{2}}} + \frac{I_o u_H(t_r)}{c(r^2 + (z - H_c^-)^2)}\right)\hat{z} \\ &- \frac{(z - H_c^+)Q_c^+}{4\pi\epsilon_o(r^2 + (H_c^+ - z)^2)^{\frac{3}{2}}}\hat{z}\end{aligned} \tag{3.29}$$

$$\frac{\partial\vec{A}}{\partial t} = -\frac{\mu_o I_o}{4\pi}\frac{1}{h(t_r) - z + \sqrt{r^2 + (h(t_r) - z)^2}}\cdot\left(\frac{\partial h(t_r)}{\partial t} + \frac{\frac{\partial h(t_r)}{\partial t}(h(t_r) - z)}{\sqrt{r^2 + (h(t_r) - z)^2}}\right)\hat{z} \tag{3.30}$$

The electric field for the isolated leader can be written directly from the terms above as:

$$\vec{E}_o(\vec{r}, t) = -\frac{\partial\phi}{\partial r}\hat{r} - \left(\frac{\partial\phi}{\partial z} + \frac{\partial\vec{A}}{\partial t}\right)\hat{z} \tag{3.31}$$

Next, we solve for the magnetic field of the isolated leader starting with (3.5).

$$\begin{aligned}\vec{B}_o(\vec{r},t) =&\vec{\nabla}\times\vec{A}(\vec{r},t)\\ =&\left(\frac{1}{r}\frac{\partial A_z}{\partial\phi}-\frac{\partial A_\phi}{\partial z}\right)\hat{r}+\left(\frac{\partial A_r}{\partial z}-\frac{\partial A_z}{\partial r}\right)\hat{\phi}+\frac{1}{r}\left(\frac{\partial rA_\phi}{\partial r}-\frac{\partial A_r}{\partial\phi}\right)\hat{z}\\ =&-\frac{\partial A_z}{\partial r}\hat{\phi}\end{aligned}$$

$$\vec{B}_o(\vec{r},t)=-\frac{\mu_o I_o}{4\pi}\left(\frac{\frac{r}{\sqrt{r^2+(H_c^- -z)^2}}}{H_c^- -z+\sqrt{r^2+(H_c^- -z)^2}}-\frac{\left(\frac{\partial h(t_r)}{\partial r}+\frac{r+\frac{\partial h(t_r)}{\partial r}(h(t_r)-z)}{\sqrt{r^2+(h(t_r)-z)^2}}\right)}{h(t_r)-z+\sqrt{r^2+(h(t_r)-z)^2}}\right)\hat{\phi} \tag{3.32}$$

3.4 Proof Of Consistency With Maxwell's Equations

Now, we must ask ourselves: Are the complicated expressions represented by (3.31) and (3.32) consistent with Maxwell's Equations or was a mistake made somewhere along the way? To ensure all is well, we will verify that (3.3), Faraday's Law, still holds before proceeding:

$$\begin{aligned}\vec{\nabla}\times\vec{E}=&-\frac{\partial\vec{B}}{\partial t}\\ \left(\frac{\partial E_r}{\partial z}-\frac{\partial E_z}{\partial r}\right)\hat{\phi}=&-\frac{\partial-\frac{\partial A_z}{\partial r}}{\partial t}\hat{\phi}\\ \left(-\frac{\partial\frac{\partial\phi}{\partial r}}{\partial z}+\frac{\partial\frac{\partial\phi}{\partial z}}{\partial r}+\frac{\partial\frac{\partial A}{\partial t}|_z}{\partial r}\right)\hat{\phi}=&\frac{\partial\frac{\partial A}{\partial t}|_z}{\partial r}\hat{\phi}\end{aligned}$$

Inspecting the expression above, it is evident that the following two equivalencies must be true for Faraday's Law to hold:

$$\frac{\partial\frac{\partial A}{\partial t}|_z}{\partial r}=\frac{\partial\frac{\partial A_z}{\partial r}}{\partial t} \tag{3.33}$$

$$\frac{\partial\frac{\partial\phi}{\partial r}}{\partial z}=\frac{\partial\frac{\partial\phi}{\partial z}}{\partial r} \tag{3.34}$$

Considering (3.34) first:

$$\frac{\partial\frac{\partial\phi}{\partial r}}{\partial z} = \frac{-I_o}{4\pi\epsilon_o v_L}\left[\frac{\frac{r}{\sqrt{r^2+(H_c^- -z)^2}}\left(1+\frac{H_c^- -z}{\sqrt{r^2+(H_c^- -z)^2}}\right)}{\left(H_c^- - z+\sqrt{r^2+(H_c^- -z)^2}\right)^2} + \frac{r\frac{H_c^- -z}{(r^2+(H-z)^2)^{\frac{3}{2}}}}{H_c^- - z+\sqrt{r^2+(H_c^- -z)^2}}\right] \tag{3.35}$$

$$+\frac{I_o}{4\pi\epsilon_o v_L}\left[\frac{\frac{\partial^2 h(t_r)}{\partial z\partial r}+\frac{\frac{\partial^2 h(t_r)}{\partial z\partial r}(h-z)+\frac{\partial h(t_r)}{\partial r}\left(\frac{\partial h(t_r)}{\partial z}-1\right)}{\sqrt{r^2+(h(t_r)-z)^2}}+\frac{\left(r+\frac{\partial h(t_r)}{\partial r}(h-z)\right)(-1)\left(\frac{\partial h(t_r)}{\partial z}-1\right)(h(t_r)-z)}{\left(r^2+(h(t_r)-z)^2\right)^{\frac{3}{2}}}}{h(t_r)-z+\sqrt{r^2+(h(t_r)-z)^2}}\right] \tag{3.36}$$

$$-\frac{I_o}{4\pi\epsilon_o v_L}\left[\frac{\frac{\partial h(t_r)}{\partial z}-1+\frac{(z-h(t_r))(1-\frac{\partial h(t_r)}{\partial z})}{\sqrt{r^2+(h(t_r)-z)^2}}}{\left(h(t_r)-z+\sqrt{r^2+(h(t_r)-z)^2}\right)^2}\left(\frac{\partial h(t_r)}{\partial r}+\frac{r+\frac{\partial h(t_r)}{\partial r}(h(t_r)-z)}{\sqrt{r^2+(h(t_r)-z)^2}}\right)\right] \tag{3.37}$$

$$-\frac{r}{4\pi\epsilon_o}\left[\frac{I_o\frac{\partial t_r}{\partial z}u_H(t_r)+I_o t_r\delta(t_r)\frac{\partial t_r}{\partial z}}{\left(r^2+(H_c^- -z)^2\right)^{\frac{3}{2}}}+\frac{I_o * t_r u_H(t_r)+Q_c^-}{\left(r^2+(H_c^- -z)^2\right)^{\frac{5}{2}}}\left(-3(z-H_c^-)\right)\right] \tag{3.38}$$

$$-\frac{r}{4\pi\epsilon_o}\left[\frac{I_o\delta(t_r)\frac{\partial t_r}{\partial z}}{c(r^2+(H_c^- -z)^2)}+\frac{I_o u_H(t_r)(-1)2(z-H_c^-)}{c(r^2+(H_c^- -z)^2)}+\frac{Q_c^+(-3)(z-H_c^+)}{(r^2+(H_c^+ -z)^2)^{\frac{5}{2}}}\right] \tag{3.39}$$

and

$$\frac{\partial\frac{\partial\phi}{\partial z}}{\partial r} = \frac{I_o}{4\pi\epsilon_o v_L}\left[\frac{\frac{r}{\sqrt{r^2+(H_c^- -z)^2}}\left(1-\frac{z-H_c^-}{\sqrt{r^2+(H_c^- -z)^2}}\right)}{\left(H_c^- - z+\sqrt{r^2+(H_c^- -z)^2}\right)^2} - \frac{r\frac{z-H_c^-}{(r^2+(H-z)^2)^{\frac{3}{2}}}}{H_c^- - z+\sqrt{r^2+(H_c^- -z)^2}}\right] \tag{3.40}$$

$$+\frac{I_o}{4\pi\epsilon_o v_L}\left[\frac{\frac{\partial^2 h(t_r)}{\partial r\partial z}-\frac{(z-h(t_r))\frac{\partial^2 h(t_r)}{\partial r\partial z}+\frac{\partial h(t_r)}{\partial r}(1-\frac{\partial h(t_r)}{\partial z})}{\sqrt{r^2+(h(t_r)-z)^2}}-\frac{\left(r+(h(t_r)-z)\frac{\partial h(t_r)}{\partial r}\right)(z-h(t_r))\left(1-\frac{\partial h(t_r)}{\partial z}\right)}{\left(r^2+(h(t_r)-z)^2\right)^{\frac{3}{2}}}}{h(t_r)-z+\sqrt{r^2+(h(t_r)-z)^2}}\right] \tag{3.41}$$

$$\frac{-I_o}{4\pi\epsilon_o v_L}\left[\frac{\left(\frac{\partial h(t_r)}{\partial r}+\frac{r+(h(t_r)-z)\frac{\partial h(t_r)}{\partial r}}{\sqrt{r^2+(h(t_r)-z)^2}}\right)\left(\frac{\partial h(t_r)}{\partial z}-1+\frac{(z-h(t_r))\left(1-\frac{\partial h(t_r)}{\partial z}\right)}{\sqrt{r^2+(h(t_r)-z)^2}}\right)}{\left(h(t_r)-z+\sqrt{r^2+(h(t_r)-z)^2}\right)^2}\right] \tag{3.42}$$

$$-\frac{z-H_c^-}{4\pi\epsilon_o}\left[\frac{I_o\frac{\partial t_r}{\partial r}u_H(t_r)+I_o t_r\frac{\partial u_H(t_r)}{\partial r}}{\left(r^2+(H_c^- -z)^2\right)^{\frac{3}{2}}}+\frac{(I_o t_r u_H(t_r)+Q_c^-)(-3)(r)}{\left(r^2+(H_c^- -z)^2\right)^{\frac{5}{2}}}\right] \tag{3.43}$$

$$-\frac{z-H_c^-}{4\pi\epsilon_o}\frac{I_o\delta(t_r)\frac{\partial t_r}{\partial r}-I_o u_H(t_r)2r}{c(r^2+(H_c^- -z)^2)^2}+\frac{3r(z-H_c^+)Q_c^+}{4\pi\epsilon_o\left(r^2+(H_c^+ -z)^2\right)^{\frac{5}{2}}} \tag{3.44}$$

Note:

$$\frac{\partial t_r}{\partial z} = \frac{z-H_c^-}{r}\frac{\partial t_r}{\partial r} \tag{3.45}$$

$$\frac{\partial u_H(t_r)}{\partial r} = \delta(t_r)\frac{\partial t_r}{\partial r} \tag{3.46}$$

$$\frac{\partial^2 h(t_r)}{\partial r \partial z} = \frac{\partial^2 h(t_r)}{\partial z \partial r} \text{ (Clairaut's Theorem)} \tag{3.47}$$

By inspecting the lines above and applying (3.45), (3.46) and (3.47) where necesarry, (3.34) holds because (3.35)=(3.40), (3.36)=(3.41), (3.37)=(3.42), (3.38)=(3.43) and (3.38)=(3.43).
Next, we will prove (3.33) holds.

$$\frac{\partial \frac{\partial A}{\partial t}|_z}{\partial r} = -\frac{\mu_o I_o}{4\pi}\frac{-\left(\frac{\partial h(t_r)}{\partial r} + \frac{r+(h(t_r)-z)\frac{\partial h(t_r)}{\partial r}}{\sqrt{r^2+(h(t_r)-z)^2}}\right)\left(\frac{\partial h(t_r)}{\partial t} + \frac{(h(t_r)-z)\frac{\partial h(t_r)}{\partial t}}{\sqrt{r^2+(h(t_r)-z)^2}}\right)}{(h(t_r)-z+\sqrt{r^2+(h(t_r)-z)^2})^2} \tag{3.48}$$

$$-\frac{\mu_o I_o}{4\pi}\frac{\frac{\partial^2 h(t_r)}{\partial r \partial t} + \frac{\frac{\partial^2 h(t_r)}{\partial r \partial t}+(h(t_r)-z)\frac{\partial^2 h(t_r)}{\partial r \partial t}}{\sqrt{r^2+(h(t_r)-z)^2}} - \frac{(h(t_r)-z)\frac{\partial h(t_r)}{\partial t}\left(r+(h(t_r)-z)\frac{\partial h(t_r)}{\partial r}\right)}{(r^2+(h(t_r)-z)^2)^{\frac{3}{2}}}}{h(t_r)-z+\sqrt{r^2+(h(t_r)-z)^2}} \tag{3.49}$$

and

$$\frac{\partial^2 A_z}{\partial t \partial r} = \frac{\mu_o I_o}{4\pi}\frac{\left(\frac{\partial h(t_r)}{\partial t} + \frac{(h(t_r)-z)\frac{\partial h(t_r)}{\partial t}}{\sqrt{r^2+(h(t_r)-z)^2}}\right)\left(\frac{\partial h(t_r)}{\partial r} + \frac{r+(h(t_r)-z)\frac{\partial h(t_r)}{\partial r}}{\sqrt{r^2+(h(t_r)-z)^2}}\right)}{(h(t_r)-z+\sqrt{r^2+(h(t_r)-z)^2})^2} \tag{3.50}$$

$$-\frac{\mu_o I_o}{4\pi}\frac{\frac{\partial^2 h(t_r)}{\partial t \partial r} + \frac{\frac{\partial^2 h(t_r)}{\partial t \partial r}+(h(t_r)-z)\frac{\partial^2 h(t_r)}{\partial t \partial r}}{\sqrt{r^2+(h(t_r)-z)^2}} - \frac{\left(r+(h(t_r)-z)\frac{\partial h(t_r)}{\partial r}\right)(h(t_r)-z)\frac{\partial h(t_r)}{\partial t}}{(r^2+(h(t_r)-z)^2)^{\frac{3}{2}}}}{h(t_r)-z+\sqrt{r^2+(h(t_r)-z)^2}} \tag{3.51}$$

By inspecting the lines above, (3.33) holds because (3.48)=(3.50) and (3.49)=(3.51). Thus, our expressions for the electric and magnetic fields satisfies Faraday's Law.

3.5 Leader Fields Above Grounded Earth

The leader propagates over a grounded plane (the earth's surface); therefore, we must consider the imaged charges and currents when solving for the electric and magnetic fields. If we are interested in the electric and magnetic fields at the earth's surface, the solution simplifies considerably. Figure 3.2 shows the real and image charge and current configuration. The net field, $\vec{E_L}$, is the sum of the actual leader field, $\vec{E_o}$, and the imaged field, $\vec{E_i}$; this results in a cancelation of the radial component and a doubling of the z component of the the isolated electric field. The net magnetic field, $\vec{B_L}$, is constructed similarly. The real current is

constructed by negative charge flowing in the negative$z$ direction; therefore, it has a positive sign pointing in the positive direction. The imaged current is constructed by positive charge flowing in the positive z direction and also has a positive sign. Referring again to Figure 3.2, using the right-hand-rule for magnetic fields and pointing the thumb in the direction of the real and imaged leader currents individually, it is evident that the sole $\hat{\phi}$ magnetic field component is doubled. The electric and magnetic fields at the earth's surface are shown in (3.52) and (3.53); and explicitly further below.

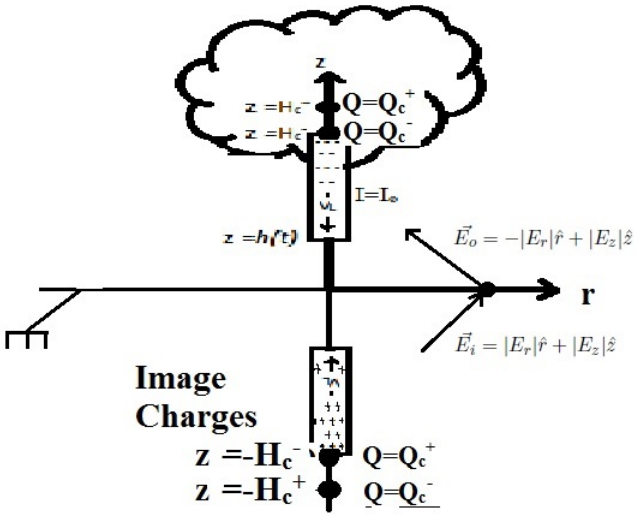

Figure 3.2: Leader source and image charge and current distribution.

$$\vec{E}_L(r, z = 0, t) = 2E_{oz}\hat{z} \tag{3.52}$$

$$\vec{B}_L(r, z = 0, t) = 2B_{o\phi}\hat{\phi} \tag{3.53}$$

$$\begin{aligned}\vec{E}_L(r,z=0,t) =& \frac{\mu_o I_o}{2\pi}\frac{1}{h(t_r)+\sqrt{r^2+h(t_r)^2}}\cdot\left(\frac{\partial h(t_r)}{\partial t}+\frac{\frac{\partial h(t_r)}{\partial t}h(t_r)}{\sqrt{r^2+h(t_r)^2}}\right)\hat{z} \\ & \frac{I_o}{v_L}\frac{1}{2\pi\epsilon_o}\frac{1}{H_c^- +\sqrt{r^2+H_c^{-2}}}\cdot\left(-1+\frac{-H_c^-}{\sqrt{r^2+H_c^{-2}}}\right)\hat{z} \\ & -\frac{I_o}{v_L}\frac{1}{2\pi\epsilon_o}\frac{1}{h(t_r)+\sqrt{r^2+(h(t_r))^2}}\cdot\left(\frac{\partial h(t_r)}{\partial z}-1+\frac{(-h(t_r))\left(1-\frac{\partial h(t_r)}{\partial z}\right)}{\sqrt{r^2+h(t_r)^2}}\right)\hat{z} \\ & +\frac{z-H_c^-}{2\pi\epsilon_o}\left(\frac{I_o\left(t-\frac{\sqrt{r^2+H_c^{-2}}}{c}\right)u_H(t_r)+Q_c^-}{(r^2+(H_c^{-2})^{\frac{3}{2}}}+\frac{I_o u_H(t_r)}{c(r^2+H_c^{-2})}\right)\hat{z} \\ & +\frac{(-H_c^+)Q_c^+}{2\pi\epsilon_o(r^2+(H_c^{+2})^{\frac{3}{2}}}\hat{z}\end{aligned} \tag{3.54}$$

$$\vec{B}_L(r,z=0,t) = -\frac{\mu_o I_o}{2\pi}\left(\frac{\frac{r}{\sqrt{r^2+(H_c^-)^2}}}{H_c^- +\sqrt{r^2+(H_c^-)^2}}-\frac{\left(\frac{\partial h(t_r)}{\partial r}+\frac{r+\frac{\partial h(t_r)}{\partial r}h(t_r)}{\sqrt{r^2+h(t_r)^2}}\right)}{h(t_r)+\sqrt{r^2+h(t_r)^2}}\right)\hat{\phi} \tag{3.55}$$

3.6 Derivation of the Delayed Height and its Derivatives

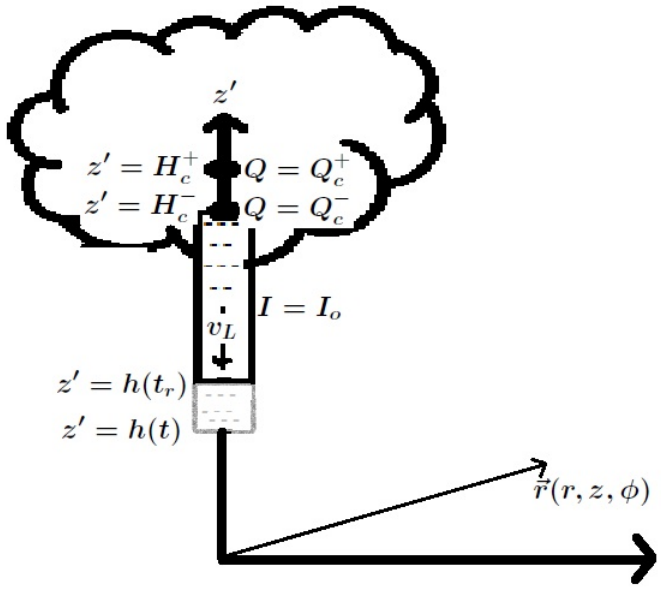

Figure 3.3: Leader height at time t and the observed height, $h(t_r)$, as seen from some position $\vec{r}$.

Our expressions for the electric and magnetic fields are exact but are not readily solvable in their current form because $h(t_r)$ still needs to be written in terms of known quantities. Referring to Figure 3.3 , it is apparent that the travel time for the leader tip to move from H_c^- to $h(t_r)$ is $\frac{H_C^- - h(t_r)}{v}$. The time it takes information to travel from the leader tip to an observer is the separation distance divided by the speed of light, $\frac{\sqrt{h(t_r)^2+r^2}}{c}$. Thus, the time an observer witnesses the leader tip at $h(t_r)$ is the sum of these terms as shown in (3.56). We can square and rearrange (3.56) in standard quadratic form as shown in (3.57) which has the solution (3.59).

$$t = \frac{H_c^- - h(t_r)}{v} + \frac{\sqrt{(h(t_r) - z)^2 + r^2}}{c} \tag{3.56}$$

$$\left(\frac{1}{v^2} - \frac{1}{c^2}\right) h(t_r)^2 + \left(\frac{2t}{v} - \frac{2H_c^-}{v^2} + \frac{2z}{c^2}\right) h(t_r) + \left(t^2 + \frac{H_c^{-2}}{v^2} - \frac{2tH_c^-}{v} - \frac{r^2}{c^2} - \frac{z^2}{c^2}\right) = 0 \tag{3.57}$$

$$h(t_r) = \frac{-\left(\frac{2t}{v} - \frac{2H_c^-}{v^2} + \frac{2z}{c^2}\right) \pm \sqrt{\left(\frac{2t}{v} - \frac{2H_c^-}{v^2} + \frac{2z}{c^2}\right)^2 - 4\left(\frac{1}{v^2} - \frac{1}{c^2}\right)\left(t^2 + \frac{H_c^{-2}}{v^2} - \frac{2tH_c^-}{v} - \frac{r^2}{c^2} - \frac{z^2}{c^2}\right)}}{2\left(\frac{1}{v^2} - \frac{1}{c^2}\right)} \tag{3.58}$$

The sign ambiguity of the discriminant, D, can be reconciled if we consider what happens in the limit that v approaches zero.

$$h(t_r) \xrightarrow{v \to 0} H_c^- - tv \pm D = h(t) \pm D$$

From Figure 3.3, it is apparent that the height observed by a distant observer cannot be smaller/shorter for a downward traveling leader; the observed height will always be larger/taller than the actual height. Hence, the negative discriminant can be discarded.

$$h(t_r) = \frac{-\left(\frac{t}{v} - \frac{H_c^-}{v^2} + \frac{z}{c^2}\right) + \sqrt{\left(\frac{t}{v} - \frac{H_c^-}{v^2} + \frac{z}{c^2}\right)^2 - \left(\frac{1}{v^2} - \frac{1}{c^2}\right)\left(t^2 + \frac{H_c^{-2}}{v^2} - \frac{2tH_c^-}{v} - \frac{r^2}{c^2} - \frac{z^2}{c^2}\right)}}{\left(\frac{1}{v^2} - \frac{1}{c^2}\right)} \tag{3.59}$$

The leader electric field is also a function of $\frac{\partial h(t_r)}{\partial t}$, $\frac{\partial h(t_r)}{\partial z}$ and the magnetitic field is a function of $\frac{\partial h(t_r)}{\partial r}$. These can be found directly from (3.59):

$$\frac{\partial h(t_r)}{\partial r} = \frac{r}{c^2\sqrt{\left(\frac{t}{v} - \frac{H_c^-}{v^2} + \frac{z}{c^2}\right)^2 - \left(\frac{1}{v^2} - \frac{1}{c^2}\right)\left(t^2 + \frac{H_c^{-2}}{v^2} - \frac{2tH_c^-}{v} - \frac{r^2}{c^2} - \frac{z^2}{c^2}\right)}} \tag{3.60}$$

$$\frac{\partial h(t_r)}{\partial t} = \frac{1}{\left(\frac{1}{v^2} - \frac{1}{c^2}\right)}\left[\frac{-1}{v} + \frac{\frac{1}{v}\left(\frac{t}{v} - \frac{H_c^-}{v^2} + \frac{z}{c^2}\right) - \left(\frac{1}{v^2} - \frac{1}{c^2}\right)\left(t - \frac{H_c^-}{v}\right)}{\sqrt{\left(\frac{t}{v} - \frac{H_c^-}{v^2} + \frac{z}{c^2}\right)^2 - \left(\frac{1}{v^2} - \frac{1}{c^2}\right)\left(t^2 + \frac{H_c^{-2}}{v^2} - \frac{2tH_c^-}{v} - \frac{r^2}{c^2} - \frac{z^2}{c^2}\right)}}\right] \tag{3.61}$$

$$\frac{\partial h(t_r)}{\partial z} = \frac{1}{\frac{1}{v^2} - \frac{1}{c^2}}\left(-\frac{1}{c^2} + \frac{\frac{1}{c^2}\left(\frac{t}{v} - \frac{H_c^-}{v^2} + \frac{z}{c^2}\right) + \frac{z}{c^2}\left(\frac{1}{v^2} - \frac{1}{c^2}\right)}{\sqrt{\left(\frac{t}{v} - \frac{H_c^-}{v^2} + \frac{z}{c^2}\right)^2 - \left(\frac{1}{v^2} - \frac{1}{c^2}\right)\left(t^2 + \frac{H_c^{-2}}{v^2} - \frac{2tH_c^-}{v} - \frac{r^2}{c^2} - \frac{z^2}{c^2}\right)}}\right) \tag{3.62}$$

Similarly, we write explicit expressions for $u_H(t_r)$ and its derviatives at $z = 0$.

$$u_H(t_r) = u\left(t - \frac{\sqrt{r^2 + (H_c^-)^2}}{c}\right)$$

$$\frac{\partial u_H(t_r)}{\partial r} = \delta\left(t - \frac{\sqrt{r^2 + (H_c^-)^2}}{c}\right)\frac{-r}{\sqrt{r^2 + (H_c^-)^2}}$$

$$\frac{\partial u_H(t_r)}{\partial z} = \delta\left(t - \frac{\sqrt{r^2 + (H_c^-)^2}}{c}\right)\frac{H_c^-}{\sqrt{r^2 + (H_c^-)^2}}$$

3.7 Leader Model Results: Leader Potentials and Fields in the Time Domain

Next, we review the time-domain model of the lightning leader beginning with scalar potential. The model developed in this thesis will be referred to as the TG model, for Thiemann-Gasiewski, to avoid confusion

Model Parameter	Value
H_c^-	7 km
H_c^+	12 km
I_o	1 kA
v	1.5 x 10^{-7}
Q_c^-	-40 C
Q_c^+	+40 C

Table 3.1: Physical values used to evaluate lightning model.

when comparing results with other models. The relevant physical parameters used as model inputs are shown in Table 3.1. Figure 3.4 shows the scalar potential prior to leader initiation. To avoid an artificial singularity at the location of the 7 km negative cloud charge which has been modeled as point charge up until now, the point charge is recast as a spherical charge of uniform density and 1 km radius, with a net charge equal to 40C. These parameters are physically consistent with cloud charge measurements as reviewed in Chapter 2. (3.26) remains unchanged at distances larger than the lower, negative cloud charge radius, R_c^-. However, at distances less than or equal to the cloud charge radius, the following modification, which is derived in most elementary electromagnetics texts (e.g. [9]), applies.

$$\frac{Q_c^-}{4\pi\epsilon_o r} \rightarrow \frac{Q_c^-}{4\pi\epsilon_o}\left(\frac{3}{2R_c^-} - \frac{r^2}{2R_c^3}\right) \tag{3.63}$$

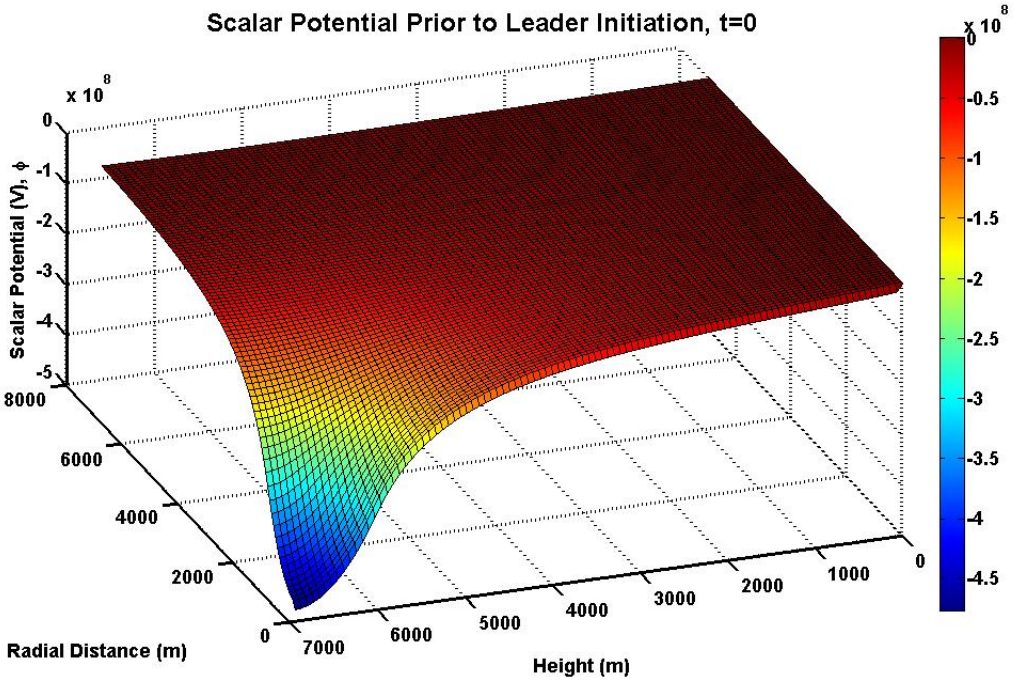

Figure 3.4: Scalar potential prior to leader initiation.

We can verify by inspection that the scalar potential is consistent with our boundary conditions as it is zero at ground ($z = 0$) and approaches zero at large radial distances. The voltage has a maximum near -500 MV at the negative cloud charge, which decreases to a still significant 1.72 kV at 70 m above ground. Comparing these results with those found in [21] and reproduced here in Figure 2.5; the peak negative voltage of -500 MV at the negative charge center is in good agreement with the -100 MV peak value shown in Figure 2.5 if we recognize that is is unlikely the balloon sounding traversed a region of maximum charge as well as the fact that the actual cloud charges were not reported in [21]. If we assume the storm in Figure 2.5 had similar charge magnitudes to those modeled here, the balloon would have been a radial distance of 2 km from the negative charge center as it traversed past. Also, this model reproduces a -50 MV value at z = 4 km (as shown in Figure 2.5) if the radial distances is again taken to be 2 km.

The change in the scalar potential from the $t = 0$ value at attachment is shown in Figure 3.5. The potential change is considered instead of the total potential because the electrostatic cloud charge, which is two orders of magnitude larger than the leader contribution, would otherwise dominate the potential due to the leader column. Again, the boundary conditions are met at ground and at large radial distances. The presence of the leader column causes a large change in voltage at positions nearby; for example, the potential change at a height and radial distance of 70 m is a approximately 12 kV. To verify the polarity is correct, first recall that only the z component of the electric field contributes to the net electric field. Therefore,

the electric field produced by the leader column must have a sign opposite the slope of the potential with respect to height. Inspecting Figure 3.5, we find the potential slope to be negative; hence the electric field will be positive, and a positive electric field is consistent with the presence of the negative charge column of a downward negative lightning strike.

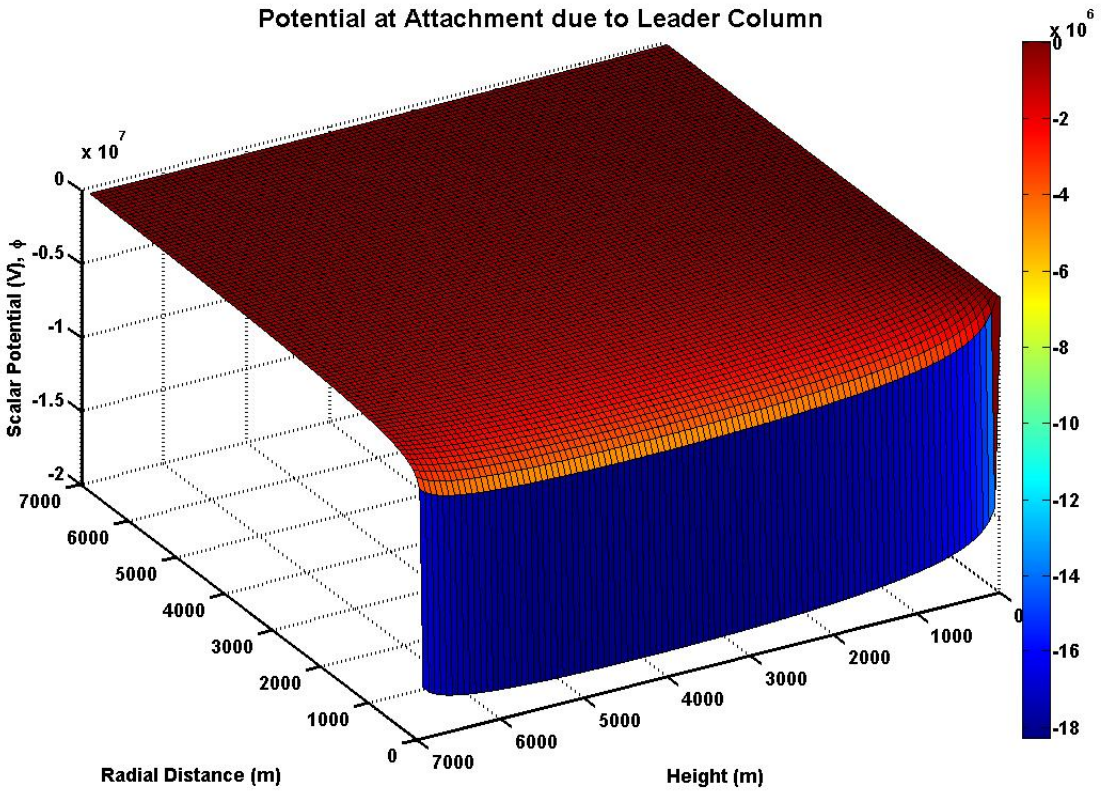

Figure 3.5: Change scalar potential at leader attachment.

The TG model results for the leader electric field are considered next. A time-series of the total electric field, including the electrostatic cloud charge, is shown at various distances in Figure 3.6. Plots of the electric field versus position at various times are shown in Figures 3.7 and 3.8; the difference between the plots being 3.8 shows the difference in the electric field from its $t = 0$ value. The selected times are fractions of total leader propagation time, $\frac{H_c^-}{v}$; specifically, $156\mu s = .33\frac{H_c^-}{v}$, $233\mu s = .5\frac{H_c^-}{v}$, $311\mu s = .66\frac{H_c^-}{v}$, $350\mu s = .75\frac{H_c^-}{v}$, $443\mu s = .95\frac{H_c^-}{v}$, $467\mu s = \frac{H_c^-}{v}$.

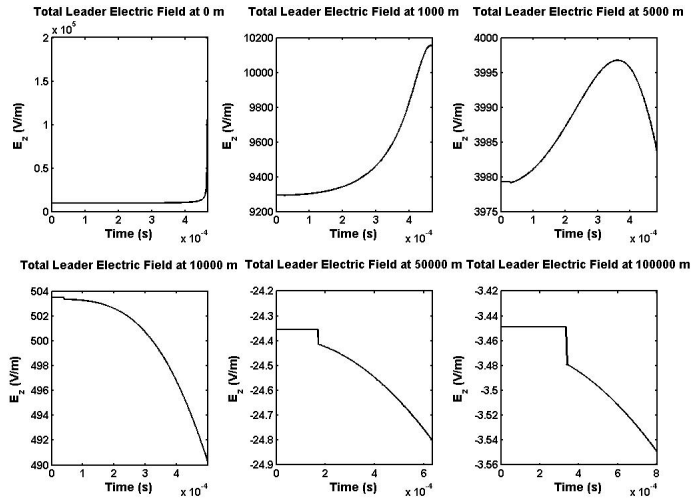

Figure 3.6: The total electric field due to the lightning leader including the electrostatic contribution of the cloud charge. Leader propagation begins at t=0 and the abscissa extends until the point of attachment.

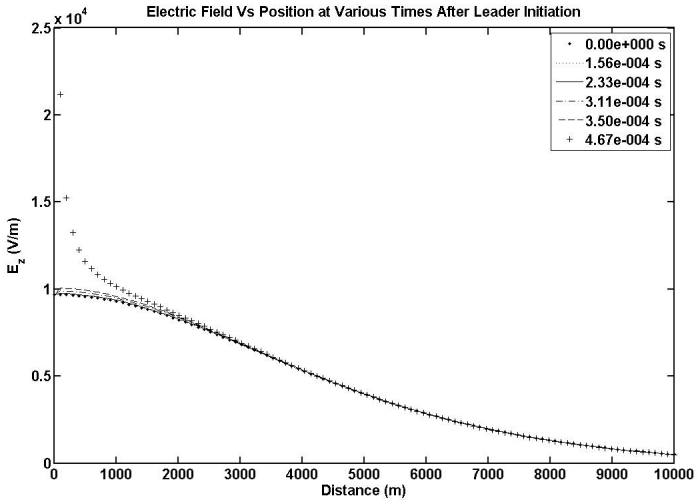

Figure 3.7: The total electric field due to the lightning leader including the electrostatic contribution of the cloud charge. The selected times are fractions of total leader propagation time, $\frac{H_c^-}{v}$; specifically, $156\mu s = .33\frac{H_c^-}{v}$, $233\mu s = .5\frac{H_c^-}{v}$, $311\mu s = .66\frac{H_c^-}{v}$, $350\mu s = .75\frac{H_c^-}{v}$, $443\mu s = .95\frac{H_c^-}{v}$, $467\mu s = \frac{H_c^-}{v}$.

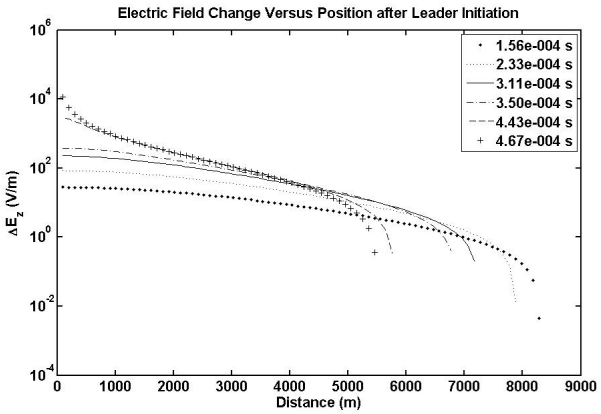

Figure 3.8: The change in electric field due to the lightning leader versus position. The selected times are fractions of total leader propagation time, $\frac{H_c^-}{v}$; specifically, $156\mu s = .33\frac{H_c^-}{v}$, $233\mu s = .5\frac{H_c^-}{v}$, $311\mu s = .66\frac{H_c^-}{v}$, $350\mu s = .75\frac{H_c^-}{v}$, $443\mu s = .95\frac{H_c^-}{v}$, $467\mu s = \frac{H_c^-}{v}$. Note, the log scale prevents negative values from being shown; so only positive electric field changes are shown.

To better understand the physical processes driving the dynamic leader field, the components of the leader field are considered separately. The electric field is decomposed into the following four components: Leader Charge, Leader Current, Cloud Drain and Cloud Discontinuity. These components are defined in (3.64) through (3.68). Figure 3.10 shows a time-series of the *change* in the electric field components from the $t = 0$ value at a series of radial distances.

$$\vec{E}_{Charge} = \frac{I_o}{v_L}\frac{1}{2\pi\epsilon_o}\frac{1}{H_c^- + \sqrt{r^2 + H_c^{-2}}} \cdot \left(-1 + \frac{-H_c^-}{\sqrt{r^2 + H_c^{-2}}}\right)\hat{z} \tag{3.64}$$

$$-\frac{I_o}{v_L}\frac{1}{2\pi\epsilon_o}\frac{1}{h(t_r) + \sqrt{r^2 + (h(t_r))^2}} \cdot \left(\frac{\partial h(t_r)}{\partial z} - 1 + \frac{(-h(t_r))\left(1 - \frac{\partial h(t_r)}{\partial z}\right)}{\sqrt{r^2 + h(t_r)^2}}\right)\hat{z} \tag{3.65}$$

$$\vec{E}_{Current} = \frac{\mu_o I_o}{2\pi}\frac{1}{h(t_r) + \sqrt{r^2 + h(t_r)^2}} \cdot \left(\frac{\partial h(t_r)}{\partial t} + \frac{\frac{\partial h(t_r)}{\partial t}h(t_r)}{\sqrt{r^2 + h(t_r)^2}}\right)\hat{z} \tag{3.66}$$

$$\vec{E}_{Drain} = \frac{-H_c^-}{2\pi\epsilon_o}\left(\frac{I_o\left(t - \frac{\sqrt{r^2 + H_c^{-2}}}{c}\right)u_H(t_r) + Q_c^-}{(r^2 + (H_c^{-2})^{\frac{3}{2}}}\right)\hat{z} \tag{3.67}$$

$$\vec{E}_{Discontinuity} = \frac{-H_c^-}{2\pi\epsilon_o}\left(\frac{I_o u_H(t_r)}{c(r^2 + H_c^{-2})}\right)\hat{z} \tag{3.68}$$

The Cloud Discontinuity field arises from the abrupt initiation of the leader. The negative point charge

located at H_c^- which serves as the source of the leader current begins to lose charge at $t = 0^+$; this sudden change in current results in a radiated pulse. However, the Continuity Equation must be satisfied, so the sudden change in current due to a reduction of negative charge at H_c^- is complemented with the arrival of negative charge at the leader tip, $h(t_r)$, resulting in a radiated pulse of opposite sign and equal magnitude evident in the Leader Charge field. The smooth portion of the Leader Charge field peaks at the attachment time for radial distances less than or equal to H_c^- with a faster rate of increase closer to t_r=0. However, as distances become much larger than H_c^-, the field peaks well before the attachment time. The Cloud Drain field is a straightforward result of the constant decrease in the source cloud charge at H_c^-. And the Leader Current term is a radiated pulse which begins to dominate at large distances.

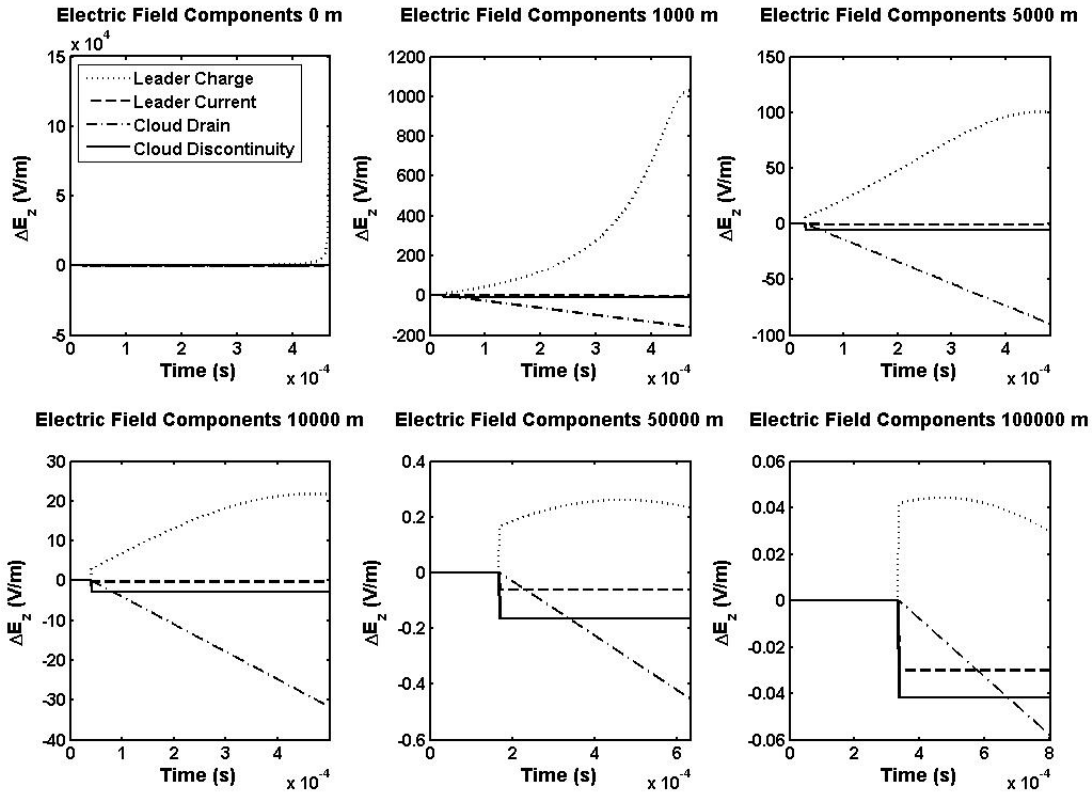

Figure 3.9: Change scalar potential at leader attachment. The abscissa ends at the (retarded) attachment time.

3.8 Comparison Against an Accepted Leader Model

In Figure 3.10, we compare the performance of the TG model with a model presented by Rakov and Uman in their contemporary lightning textbook [32]. Rakov and Uman began with an expression for the electric

field *change* developed by Thottappillil *et al* in [39] shown in (3.69) below and solve it with the assumption that retardation effects are negligible and that charge density is uniform; their solution is shown in (3.70). Note that a negative sign was added to the expression presented in [32] for consistency with the convention used in this paper; Rakov and Uman use the *atmospheric convention* which defines a positive electric field as pointing downward. Note that many workers in the field have chosen to use the atmospheric sign convention, but this thesis uses the conventional "physics" convention and *all* TG model results in this thesis are presented using this convention to avoid confusion. Rakov and Uman present the magnetic field expression (3.71) in [32] taken from [41]. This formulation again neglects retardation effects and is compared with the exact expression for the magnetic field developed here in Figure 3.11.

$$E_z(r,t) = \frac{1}{2\pi\epsilon_o}\int_{h(t_r)}^{H_c^-}\frac{z'}{s^3}\rho_L(z',t_r)dz' - \frac{1}{2\pi\epsilon_o}\frac{H_c^-}{\left((z-z')^2+(r-H_c^-)^2\right)^{\frac{3}{2}}}\int_{h(t_r)}^{H_c^-}\rho_L(z',t_r)dz' \tag{3.69}$$

$$E_z(r,t) = -\frac{\rho_L}{2\pi\epsilon_o r}\left[\frac{1}{\sqrt{1+\frac{(H_c^- - vt)^2}{r^2}}} - \frac{1}{\sqrt{1+\frac{(H_c^-)^2}{r^2}}} - \frac{(H_c^- - (H_c^- - vt))H_c^-}{r^2\left(1+\frac{(H_c^-)^2}{r^2}\right)^{\frac{3}{2}}}\right] \tag{3.70}$$

$$B_\phi(r,t) = \frac{-\mu_o}{2\pi r}\left[\frac{H_c^-}{\sqrt{r^2+(H_c^-)^2}} - \frac{H_c^- - vt}{r^2+(H_c^- - vt)^2}\right] \tag{3.71}$$

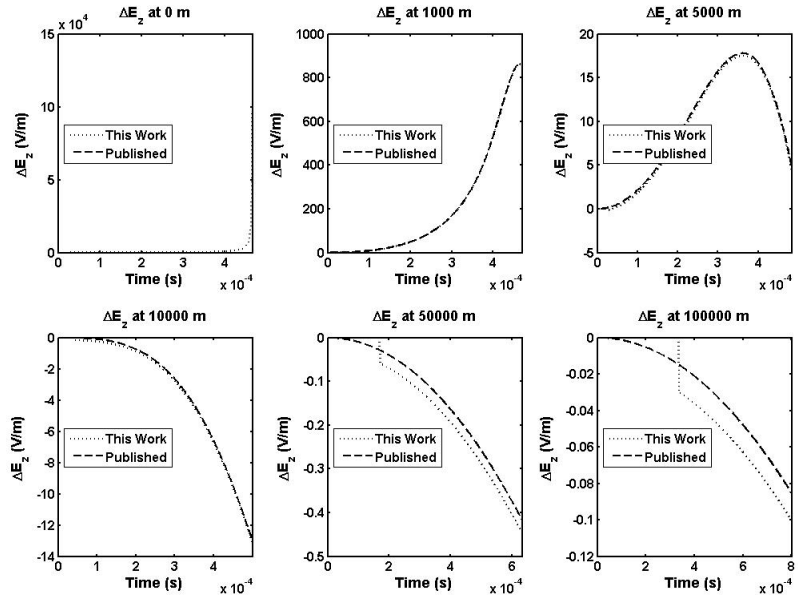

Figure 3.10: This series of plots shows the change in electric field for the TG model versus time at different distances compared with a previously published field model given by (3.70). The negative charge height is 7km, the positive charge height is 12 km, both with initial magnitude equal to 40C. The leader peak current was taken to be 1 kA with a velocity of $1.7x10^7 \frac{m}{s}$.

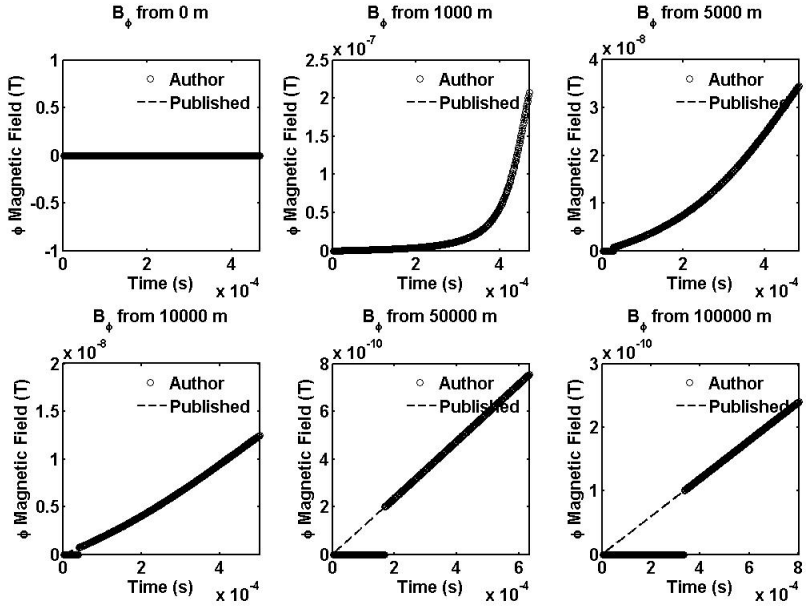

Figure 3.11: This series of plots shows the change in magnetic field versus time at different distances. The TG model fields are compared with previously published fields given by (3.71). The negative charge height is 7km, the positive charge height is 12 km, both with initial magnitude equal to 40C. The leader peak current was taken to be 1 kA witha velocity of $1.7x10^7 \frac{m}{s}$.

Chapter 4

Electromagnetic Fields of the Complete Strike Sequence

In this section, we develop a numerical model for the return stroke portion of the lightning strike sequence and combine it with the leader model developed in the preceding section. The total strike TG (Thiemann-Gasiewski) model is then compared against measured lightning electric and magnetic fields. Existing, published lightning strike models are reviewed and compared against the total strike model.

4.1 Return Stroke Model Development

The return stroke charge configuration is shown in Figure 4.1 and is a superposition of the column of charge left by the leader with line charge density, λ_L, and an upward propagating neutralization charge with equal and opposite line charge density. The return stroke charge density is shown in (4.2) below in terms of the leader line charge, λ_L, the negative cloud charge height, H_c^-, and the height of the return stroke tip, h_{rs}.

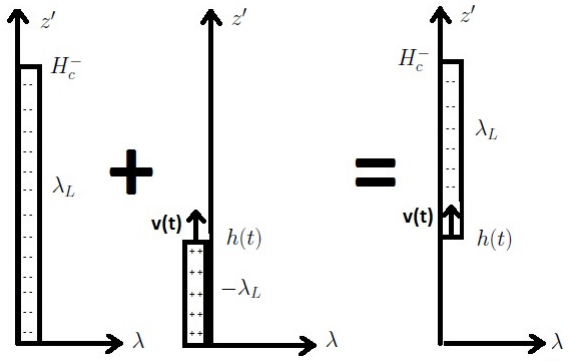

Figure 4.1: The return stroke charge is the sum of the negative charge column left by the leader and the upward propagating positive charge which neutralizes the leader charge.

$$\lambda_L = \frac{-I_o}{v_L} \tag{4.1}$$

$$\rho_{rs}(\vec{r'}, t) = \lambda_L \left[u(H_c^- - z') - u(h_{rs}(t) - z')\right] \delta^2(r') \tag{4.2}$$

We can use the Continuity Equation, (3.22), to determine the current density.

$$\begin{aligned} -\frac{\partial \rho(r', t)}{\partial t} &= \nabla \cdot J_{rs}(r', t) \\ -\lambda_L \delta(h_{rs}(t) - z') v(t) &= \nabla \cdot J_{rs}(r', t) \\ \int -\lambda_L \delta(h_{rs}(t) - z') v(t) dz' &= J_{rs,z}(r', t) \\ -\lambda_L v(t) u(h_{rs}(t) - z') + C &= J_{rs,z}(r', t) \end{aligned} \tag{4.3}$$

We can solve for the constant in (4.3) by applying the boundary condition of zero current at the cloud charge height, H_c^-. The resulting current density is shown in (4.5) below and Figure 4.2. The return stroke current density is upward propagating and serves to transport positive charge to the position h(t) neutralizing the negative charge left by the leader.

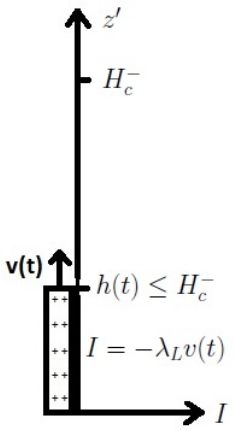

Figure 4.2: The return stroke current serves to transport charge to neutralize the leader column.

$$C = \lambda_L v(t) u(h(t) - H_c^-) \tag{4.4}$$

$$J(\vec{r'}, t) = \lambda_L v(t) \left[u(h(t) - H_c^-) - u(h(t) - z') \right] \delta^2(r') \tag{4.5}$$

To find the electric and magnetic fields, we follow the same process used to determine the leader fields, first solving for the vector and scalar potentials at the retarded time using, (3.12) and (3.13), and then plugging these values into (3.5) and (3.7) to get the electric and magnetic emissions. Note that this will give us the potentials for an isolated return stroke, and we can account for the affect of the ground plane using the same symmetry arguments in (3.52) and (3.53). The return stroke scalar potential will have a similar solution to that of the leader scalar potential, but we run into trouble solving for the vector potential, which is shown in (4.6), due to the time varying velocity evaluated at the retarded time. This author found no known solutions to integrals of this form, and therefore the return stroke electric and magnetic fields cannot be written in closed form and must be solved for numerically. The numerical solutions to the isolated (no ground plane) return stroke vector and scalar potentials are shown in Figures 4.3 and 4.4 below at various distances. Numerical space and time derivatives are taken of these potentials to find the electric and magnetic fields which are shown in Figures 4.5 through 4.9. Note that the distinct downward pulse at the end of the magnetic field in Figure 4.7 is due to the abrupt turning off of the velocity, which is proportional to current, once the return stroke wavefront reaches the cloud top. If the return stroke velocity were allowed to gradually decrease with height as is what likely occurs in nature, this pulse would not occur and the gradual hump that is evident in magnetic field observations such as Figure 1.5 would appear in the TG model. Because of the unphysical nature of this pulse, the magnetic field is replotted, omitting the pulse, in Figure 4.8.

$$\vec{A}(r,z,t) = \frac{\lambda_L \mu_o}{4\pi} \int_0^{H_c^-} \frac{v_{rs}(t - \frac{\sqrt{r^2+(z-z')^2}}{c}) \left[u(h(t - \frac{\sqrt{r^2+(z-z')^2}}{c}) - H_c^-) - u(h(t) - z') \right]}{\sqrt{r^2 + (z-z')^2}} dz\hat{z} \tag{4.6}$$

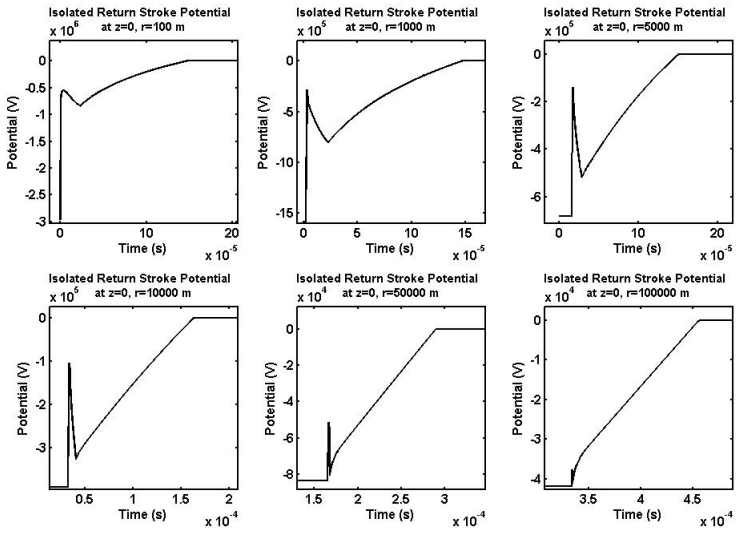

Figure 4.3: Numerical solutions for the return stroke scalar potential at various distances. These solutions are for the isolated return stroke, meaning there is no ground plane at z=0. The z=0 electric and magnetic fields with a ground plane present can be found using the isolated solution with symmetry arguments.

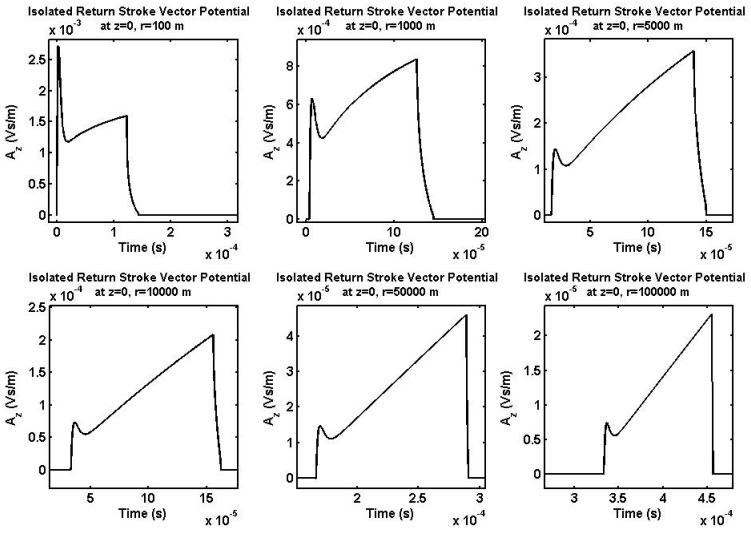

Figure 4.4: Numerical solutions for the return stroke vector potential at various distances. These solutions are for the isolated return stroke, meaning there is no ground plane at z=0. The z=0 electric and magnetic fields with a ground plane present can be found using the isolated solution with symmetry arguments.

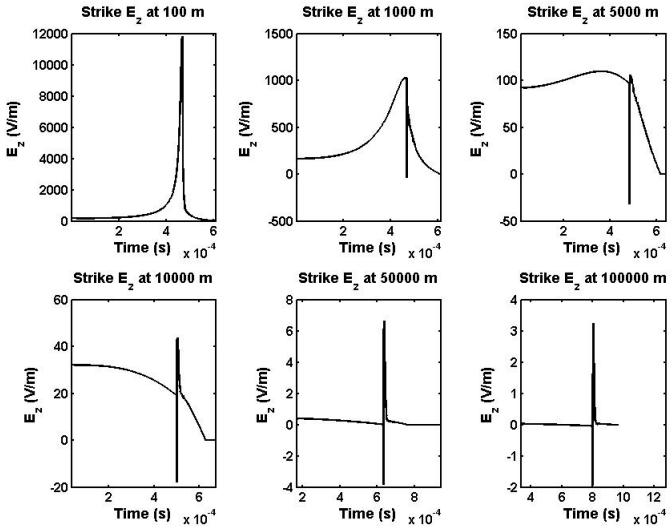

Figure 4.5: The modeled electric field at various distances versus time for the dart leader and subsequent return stroke. The field due to the static cloud charge, as shown in Figure 3.6, has been removed to highlight the emissions due to dynamic processes. The dart leader emission model is the analytical model shown earlier in this work using the same parameters as in Figure 3.10. The return stroke emissions are modeled numerically using the velocity in (5).

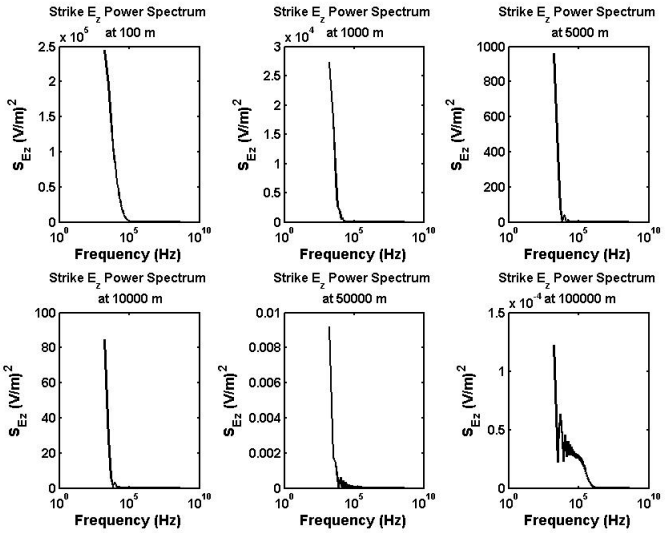

Figure 4.6: The power spectrum of the electric field shown in Figure 4.5.

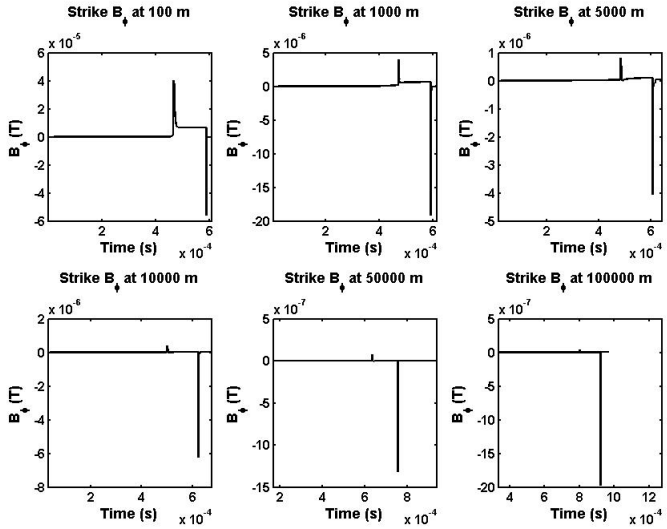

Figure 4.7: The modeled magnetic field at various distances versus time for the dart leader and subsequent return stroke. The second pulse is due to the unphysical nature of the return stroke velocity modeled by (5) which travels at a significant fraction of the speed of light when it abruptly stops at a height of 7km above ground.

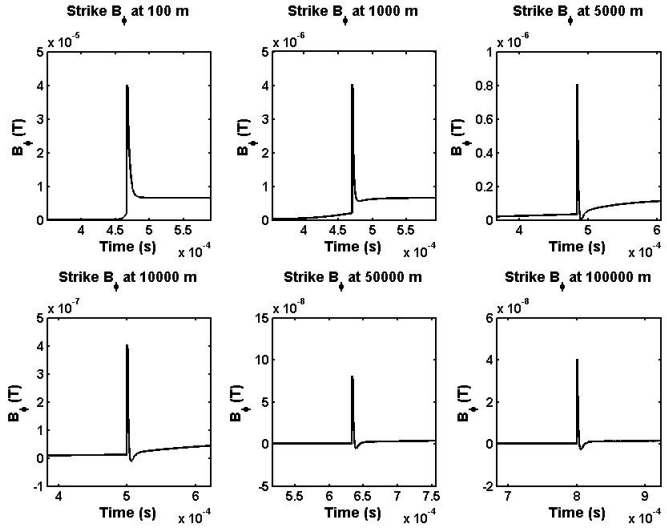

Figure 4.8: The modeled magnetic field at various distances versus time for the dart leader and subsequent return stroke. This is the same field as in Figure **??** but the second, unphysical pulse is neglected. The dart leader emission model is the analytical model shown earlier in this work using the same parameters as in Figure 3.10. The return stroke emissions are modeled numerically using the velocity in (5).

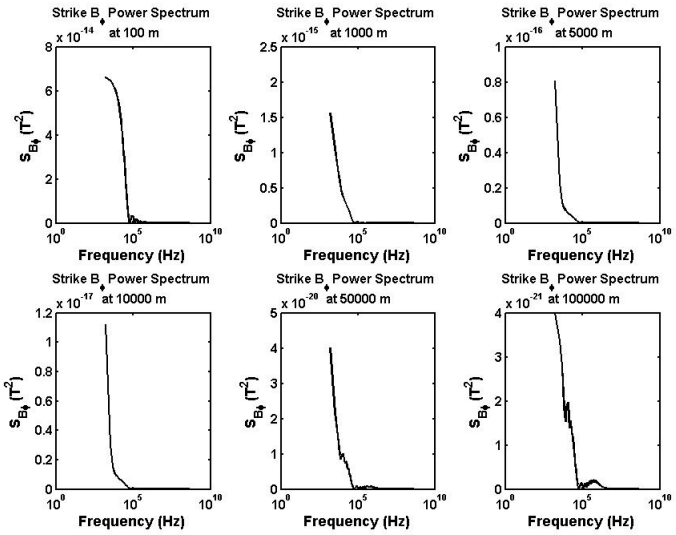

Figure 4.9: The power spectrum of the magnetic field shown in Figure 4.8.

The initial downward spike evident in the modeled return stroke electric field is shown in detail in Figure 4.10 and is due to the increasing return stroke velocity. The abrupt drop from 95 V/m to 0 V/m is a result of the modeled velocity's non-zero initial value, and had the velocity model started smoothly from zero, the box-car at the leader-return stroke interface would be smooth. As the return stroke velocity decreases, the electric field begins to increase. This sign dependence on the velocity derivative can be explained by vector potential being proportional to velocity through the current; the electric field depends on the time derivative of the vector potential which, thus, depends on the time derivative of the velocity.

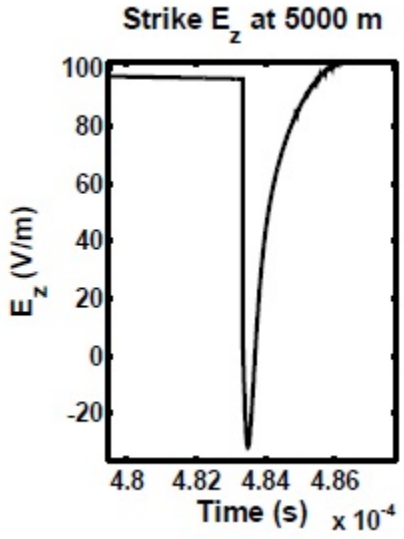

Figure 4.10: A detailed view of the downward pulse in the 5000 m electric field from Figure 4.5.

4.2 Model Comparisons with Observations

Comparing the TG model results to the measured electric and magnetic fields in Figure 1.5, the first dissimilarity is that the downward pulse is not observed in the measurements. One explanation may be that these measurements were band limited and unable to resolve the downward pulse. The measurements in [17] were made with a system that had a 1 MHz bandwidth with a Nyquist limited resolution of .5 μs and the FWHM of the pulse in Figure 1.5 is .7 microseconds; thus this pulse would be barely resolvable and consist of 2 or 3 samples. Further, the leader contribution was omitted from these measurements so the downward pulse would have occurred in the first few samples and may have also been omitted and/or normalized to the arbitrary ordinate axis. The downward pulse has been observed in another published measurement as shown in Figure 4.11 [24], however, this data is at too course of resolution to compare the fine structure of the waveforms. A second distinct feature in Figure 1.5 which is not observed here is the upward ramp which

occurs after the waveform. This ramp is believed to be caused by transverse currents carrying the return stroke neutralization charge from the channel inner core to the outside of the sheath as discussed in Chapter 2. The post peak hump shown in Figure 1.5 is also not evident in the model and may be due to lightning behavior or waveform propagation effects not included in the model.

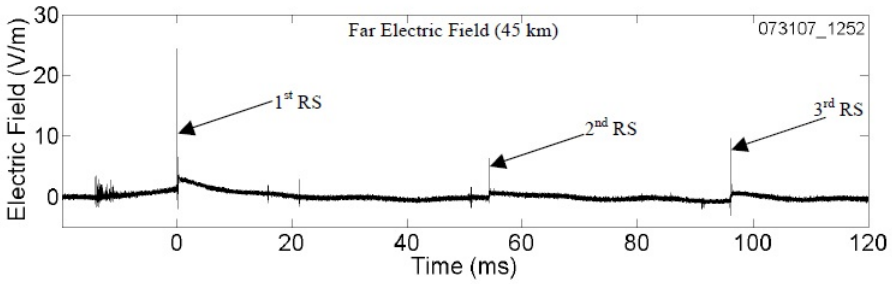

Figure 4.11: Course resolution electric field measurements of 3 return strokes at 45 km showing sharp pulses in both directions consistent with the model results of this thesis. Adapted from [24].

An important similarity in these model results with the data shown in 1.5 is the magnitudes of the modeled fields agree quite well acknowledging that variable parameters such as current determine the peak fields. The data (model) show the peak from initial value electric and magnetic fields at 10 km to be 30 (20) V/m and 2 $\times 10^{-7}$ (4 $\times 10^{-7}$) T and, at 50 km, 7 (7) V/m and 2×10^{-8} (8×10^{-8}) T, respectively. A second similarity is in the agreement of the pre-hump magnetic field waveform shape which both show a trough after the initial peak. Data which includes the full leader and return stroke emissions demonstrate more recognizable features with the model such as the 477 m electric field measurements shown in Figure 4.12 which resembles the 1000 m model electric field waveform. The 12 km leader return stroke waveform shown in Figure 5 agrees well with the 5 km model data. Both show an initial gradual hook shape due to the leader, followed by an abrupt drop due to the return stroke; the downward impulse due to return stroke in Figure 5 is likely suppressed due to a 10 μs moving average of the presented data.

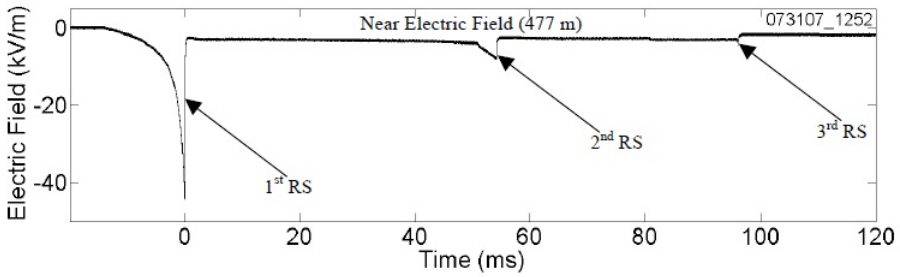

Figure 4.12: Course resolution electric field measurements of 3 return strokes at 477 m. Note the electric field sign convention is opposite that used in this thesis and the positive electric field points away from the cloud in this data. Adapted from [24].

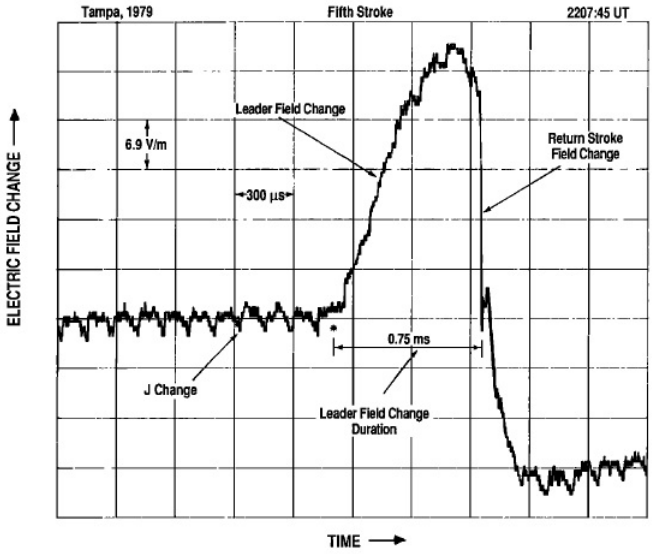

Figure 4.13: 10 μs averaged data of the leader and return stroke electric field at 12 km. Adapted from [29].

Figure 4.14 shows electric field emissions at 60 m and 550 m of leader and return strokes from rocket triggered lightning experiments. These data show many of the same features evident in the 100m and 1000m modeled data shown in Figure 4.5 which has been reproduced in a detail view in Figure 4.15. Note that the sign convention in Figure 4.14 is opposite that used in this thesis. Both the data and model show similar gradual leader waveforms and a sharp pulse due to the return stroke. Also, the magnitudes are in close agreement as are the overall change in field caused by the strike. On the other hand, comparisons of magnetic field waveforms from triggered lightning measured at 60 m show less similarity with the modeled magnetic field as shown in Figures 4.16 and 4.17 [44]. This is likely due to the dominant role the return stroke plays in magnetic field waveforms, even at close distances. As was mentioned above, the return stroke velocity time dependence influences the shape of the magnetic field waveform and any inaccuracies in the

return stroke velocity will be reflected in the magnetic field waveforms.

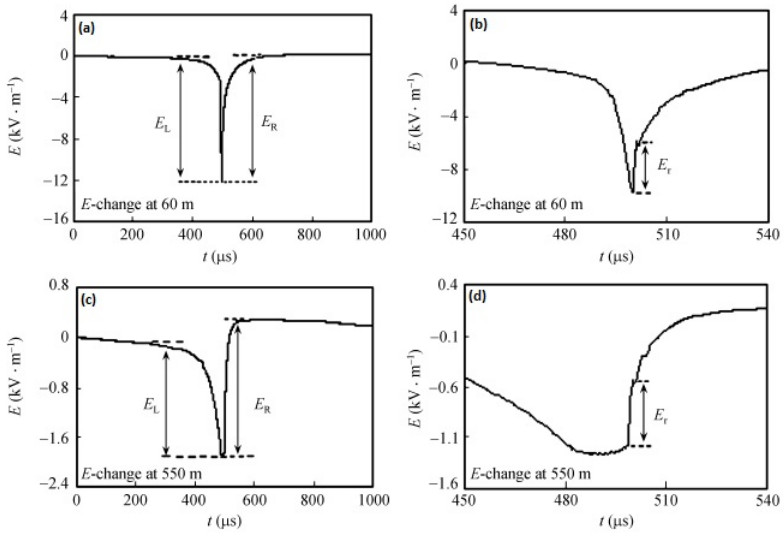

Figure 4.14: Electric field measurements of triggered lightning at 60 m ((a) and (b)) and 550 m ((c) and (d)). (b) and (d) are higher resolution presentations of the data in (a) and (c) respectively. Note the data shown here uses the opposite sign convention as this thesis. E_R and E_L indicate the return-stroke and leader contributions, respectively and E_r is defined as the "peak" radiation field in [27]. Adapted from [27].

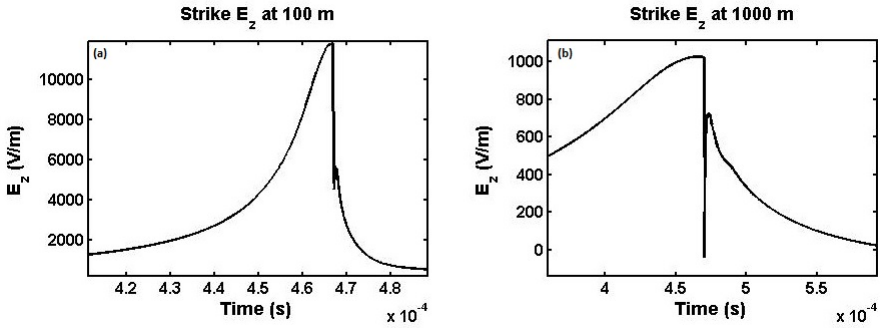

Figure 4.15: 100 m and 1000 m modeled electric fields from Figure 4.5 for comparison with measurements in Figure 4.14 (b) and (d).

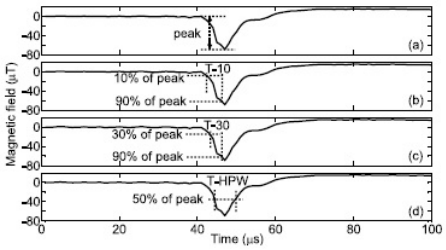

Figure 4.16: Magnetic field measurements of triggered lightning at 60 m. Note the data shown here uses the opposite sign convention as this thesis. Adapted from [44].

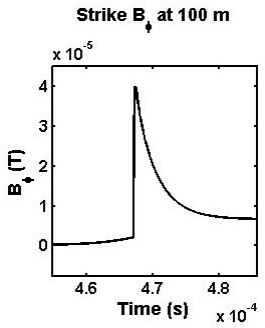

Figure 4.17: 100 m modeled magnetic fields from Figure 4.7 for comparison with measurements in Figure 4.16.

4.3 Model Comparisons with Existing Lightning Models

Lightning models have been classified into four categories in [31] and [32] which are Gas Dynamic, Electromagnetic, Distributed Circuit and Engineering Models. The gas dynamic models consider the radial evolution of the plasma in the lighting channel and largely avoid the longitudinal dynamics. These models determine properties such as temperature, pressure and radiated optical power by evaluating the interactions of the constituent ions and electrons in the plasma. The class of Electromagnetic models treat the lightning channel as a lossy thin wire and use this to determine the charge and current distributions in the channel and associated radiated fields through numerical solutions to Maxwell's Equations. The Distribute Circuit models are a simplification of the Electromagnetic models and treat the lightning channel as a transmission line with a prescribed resistance, inductance and capacitance. The Telegrapher's Equations are solved to determine the voltage and current on the channel, from which the electric and magnetic emissions can be determined. The class of Engineering models have approximately 2 or 3 variable parameters and prescribe the lightning current based on physical observations and then solve for the electromagnetic emissions, often adjusting parameters such as velocity so that the models are in better agreement with the observed emissions. The Engineering models are most commonly used in the literature to model lightning emissions and are most similar to the model developed in this thesis; therefore, they warrant a more detailed review.

Engineering models typically have the form shown in (4.7) where the first term, $u(t - z'/f)$, is the Heaviside step function; $P(z', t)$ is an attenuation factor; and $I(0, t - z'/v)$ is the return stroke current.

$$I(z', t) = u(t - z'/v_f)P(z', t)I(0, t - z'/v) \tag{4.7}$$

The parameters v_f and v are the return stroke wave-front velocity and the current wave velocity which can be different. Table 4.1 shows the choice of attenuation factors and velocities for five published models.

Model	$P(z',t)$	v
TL [40]	1	v_f
MTLL [30]	$1-\frac{z'}{H}$	v_f
MTLE [25]	$\exp\left(-\frac{z'}{\lambda}\right)$	v_f
MTLD [1]	$\left[1-\exp\left(-\frac{t-z'/v_f}{\tau}\frac{\lambda_p}{z'}\right)\right]\left(1-\frac{z'}{H}\right)$	v_f
TCS [10]	1	$-c$

Table 4.1: Parameters from a number of return stroke engineering models. Adapted from [31].

Engineering models can be further divided into two subclasses which are shown graphically in Figure 4.18: Every model in Table 4.1 except the TCS model is of the *Transmission Line* (TL) subclass; these models assume the current source is located at the lightning channel base (at ground level) and fixed, and current flows upward from the base. The second model subclass is the *Traveling Current Source* (TCS) subclass; as the name implies, the current source travels with the wavefront and current flows downward into the channel from the wavefront. Considering the specific TCS model in Table 4.1, the current source travels with the return stroke wavefront upwards at $v_f < c$ and sources current downward with a velocity of c.

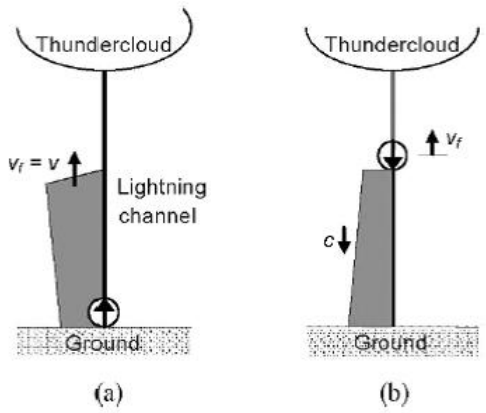

Figure 4.18: Engineering models can be classified as being one of two types, Transmission Line or Traveling Current Source, depending on where the model locates the current source. Adapted from [31].

Engineering models can be implemented to account for the radial current which flows outward from the channel core to neutralize the charge left by the leader. This can be done by discretizing the vertical height of the model, and adding a horizontal leg to the circuit with a 1 m length which is the approximate width of the corona sheath as is shown in Figure 5. As the return stroke wave-front reaches each discrete height, a switch is closed allowing current to flow radially. Depending on whether this is a TL (Figure 5.a) or TCS

(Figure5.b) type model, the current will flow towards or away from the corona sheath.

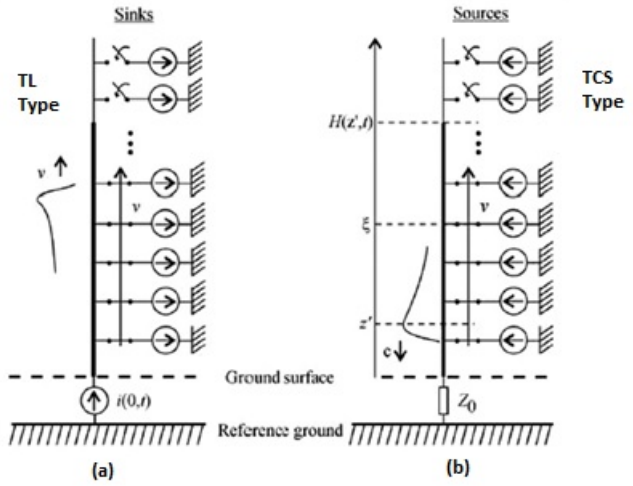

Figure 4.19: Engineering models can account for radial flow through numerical implementation and the sign of the radial flow depends on whether the model is TL or TCS type. Adapted from [31].

The engineering models determine only the current and rely on other models and methods to determine the electromagnetic emissions from the current. Rakov and Uman are proponents of a set of equations which are exact solutions to Maxwell's Equations for a return stroke in [32], [41], [31] and [39] and given their authoritative position in the field, these equations appear throughout the literature. These equations are shown in (4.8) and (4.9) below with the geometry defined in Figure 4.20. A search through the literature for the origin of these equations, shows the exact solution to Maxwell's Equations for lightning emissions depends on approximating the lightning leader or return stroke as a dipole antenna [22] and solving for the transient emissions associated with *forming* a finite electrostatic dipole. In other words, the situation in which charge $+Q$, located at height $z' = H$ at $t = 0$, is lowered to height $z' = 0$ at $t = T$ can be treated as the formation of a dipole, $q(z', 0 < t < T) = -Q\delta(z' - H) + Q\delta(z')$. The engineering models presented in Table 4.1 are modeled in [39] where (4.8) is used to calculate the electric field; and model results are presented along with measurements for a 50 m radial distance. These results are compared against the TG return stroke model developed in this thesis in Figure 4.21 and it is apparent that the TG model performs better than a number of the other models and comparable to the best models, TCS and DU, at 50 m.

$$
\begin{aligned}
E_z(r,t) = {} & \frac{1}{2\pi\epsilon_o}\int_0^{H(t)} \frac{2z'^2 - r^2}{R^5(z')} \int_{\frac{z'}{v_f}+\frac{R(z')}{c}}^{t} I(z', \tau - R(z')/c)\, d\tau\, dz' \\
& + \frac{1}{2\pi\epsilon_o}\int_0^{H(t)} \frac{2z'^2 - r^2}{cR^4(z')} I(z', \tau - R(z')/c)\, dz' \\
& - \frac{1}{2\pi\epsilon_o}\int_0^{H(t)} \frac{r^2}{cR^3(z')} \frac{\partial I(z', \tau - R(z')/c)}{\partial t} dz' \\
& - \frac{1}{2\pi\epsilon_o} \frac{r^2}{c^2 R^3(H(t))} I(H(t), v_f) \frac{dH(t)}{dt}
\end{aligned}
\tag{4.8}
$$

$$B_\phi(r,t) = \frac{\mu_0}{2\pi}\int_0^{H(t)}\left[\frac{r}{R^3(z')}I(z',t-R(z')/c) + \frac{r}{cR^2(z')}\frac{\partial I(z',t-R(z')/c)}{\partial t}\right]dz' \qquad (4.9)$$
$$+ \frac{\mu_0}{2\pi}\frac{r}{cR^2(H(t))}I(H(t),H(t)/v_f)\frac{dH(t)}{dt}$$

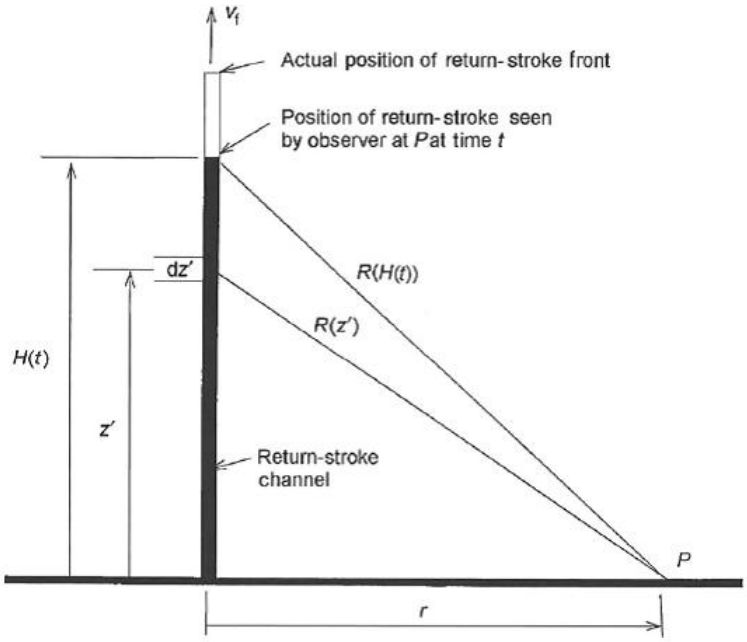

Figure 4.20: Geometry used in equations (4.8) and (4.9). Adapted from [39].

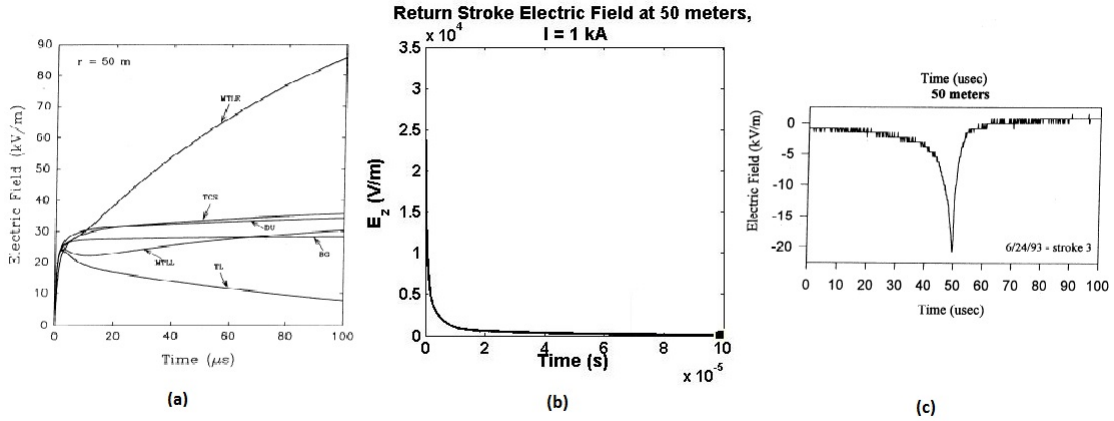

Figure 4.21: A comparison of the predicted electric field at 50 m by published engineering models (a) with the TG model (b) and measured emissions (c). Note that (a) and (c) use an opposite sign convention that (b) for positive electric field. (a) and (c) adapted from [39].

Chapter 5

Conclusion

A complete derivation of the TG model has been presented. The model was independently derived and relied on physical inputs consistent with observation. The model has been validated by comparison with existing models as well as measurements which have shown the model predictions to be within reasonable agreement with expected values. Other models have been briefly reviewed and evidence has been presented which suggests the TG model may more accurately predict lightning waveforms.

The initial intent of this work was not to seek out a model which has not been published; instead it was to gain a detailed understanding of the electromagnetics of a lightning strike, and this was approached by setting up a simple problem and modeling it independently rather than transcribing the work of others. The assumption had been that when the independent derivation and analysis were complete, there would be a very similar published model with which to compare; and it is possible that there is and this author has yet to uncover it. The TL model first derived in [40] presents the exact magnetic field formalism for the return stroke; but does not offer a closed form solution because of the exponential velocity dependence. It may be because the return stroke dominates the waveform at large distances, careful consideration of the VLF *leader* emissions have been neglected by the community because of their diminished utility. Clearly, the framework for an exact solution to the magnetic field was presented in [40] but the authors pursued the more difficult problem of solving for the emissions of the return stroke with its exponentially varying velocity rather than the constant velocity dart leader.

The conventional set of equations for the electric and magnetic fields, (4.8) and (4.9), which approximate the return stroke as a dipole antenna, appears to perform well for the more complicated models such as the TCS and DU models, but not as well for the simpler TL model. The discrepancy is likely not due to the traveling current source models more accurately depicting the physics of the return stroke because there is no evidence to suggest that the return stroke current actually is sourced downward at the speed of light

from the leader tip. The TCS model was originally proposed to improve discrepancies in the TL model when using (4.8) [10]. It is unclear whether these same discrepancies would be evident if the TG model approach had been used but the example in Figure 4.21 suggests otherwise considering the current structure in the TG and TL models are very similar.

The simplest way to increase location accuracy would be to reduce the sensor baselines which would result in an increased contribution by the leader to the measured waveforms. This may become prohibitively expensive over the entire country, but could be economically feasible over a smaller region of concern; for example, an area with high property density that is prone to lightning fires, like much of Colorado's front range, could warrant a higher density network. A 400 km^2 area could be covered by 9 sensors with 10 km baselines which could be coordinated over the Internet using cellular service. In such a small scale network, the leader waveforms will play a larger role in determining the waveform shape and therefore need to be well understood. An example data processing algorithm for a waveform such as the one shown in Figure could first use the leader waveform to correlate received waveforms with a particular strike, and then use "notch" due to the return stroke as the fiduciary to determine precise timing for the TOA algorithm.

A number of improvements can be made to the TG model which may improve its accuracy. The TG model provides a platform to test velocity models, following the example of previous workers as discussed in [8]. The existing velocity model could be corrected by having a zero starting and ending velocity by modifying , or the velocity model developed by Cooray and shown in Figure could be used. The resulting waveforms can then be compared to measured waveforms to determine the validity of the velocity change. Another improvement would be to implement the TG model return stroke as is shown in Figure to account for the radial flow of the corona currents. The existing solution to Maxwell's equations would need to be reviewed because the horizontal currents will lead to a horizontal vector potential and more terms will need to be accounted for.

In closing the TG model provides a framework to study lightning emissions at relatively close distances where the leader contributes significantly to the waveform and ground losses are negligible. The TG model can also be used to evaluate return stroke velocity profiles; and the TG model method of solving for electric and magnetic emissions directly from Maxwell's Equations may be superior to the current method of applying a dipole approximation to the leader channel. Given the need to numerically solve for the current in most models and the availability of inexpensive computing resources, the additional need to solve Maxwell's Equations numerically is an acceptable cost if it reduces current model complexity and results in more accurate predictions.

Chapter 6

Bibliography

[1] Y. Baba and M. Ishii. Lightning return stroke model incorporating current distortion. *IEEE Trans. Electromagn. Compat.*, 44:476–478, 2002.

[2] B. Baker, M.B. Baker, E.R. Jayaratne, J. Latham, and C.P.R. Saunders. The influence of diffusional growth rates on the charge transfer accompanying rebounding collsions between ice crystals and soft hailstones. *Q.J.R. Meteor. Soc.*, 113:1193–1215, 1987.

[3] H.-D. Betz, K. Schmidt, P. Oettinger, and M. Wirz. Lightning detection with 3-d discrimination of intracloud and cloud-to-ground discharges. *Geophysical Research Letters*, 31(L11108):1–4, 2004.

[4] C.E.R Bruce and R.H. Golde. The lightning discharge. *J. Inst. Elec. Engrs. (London)*, 88(2):487–505, 1941.

[5] V. Cooray. A model for subsequent return strokes. *Journal of Electrostatics*, 30:343–354, 1993.

[6] K.L. Cummins and M.J. Murphy. An overview of lightning locating systems: History, techniques, and data uses, with an in-depth look at the us nldn. *IEEE Trans. Electro. Compat.*, 51(3):499–518, 2009.

[7] I. Gallimberti. The mechanism of long spark formation. *Journal De Physique*, 40(C7):193–250, 1979.

[8] C. Gomes and V. Cooray. Concepts of lightning return stroke models. *IEEE Trans. on Electromag. Comp.*, 42(1):82–96, 2000.

[9] David J. Griffiths. *Introduction to Electrodynamics*. Prentice Hall, third edition, 1999.

[10] F. Heidler. Traveling current source model for lemp calculation. *Proc. 6th Int. Zurich Symp. Electromagn. Compat., Zurich, Switzerland*, pages 157–162, 1985.

[11] V.P. Idone and R.E. Orville. Lightning return stroke velocities in thunderstorm research international program. *J. Geophys. Res.*, 87(C7):4903–4915, 1982.

[12] E.A. Jacobson and E.P. Krider. Electrostatic field changes produced by florida lightning. *J. Atmos. Sci.*, 33:113–117, 1976.

[13] J.R. Johler, W.J. Kellar, and L.C. Walters. Phase of the low radio frequency ground wave. *National Bureau of Standard Circular*, 573:1–40, 1956.

[14] P.R. Krehbiel. *An analysis of electric field change produced by lightning.* PhD thesis, University of Manchester Institute of Science and Technology, 1981.

[15] P.R. Krehbiel, M. Brook, and R.A. McCrory. An analysis of the charge structure of lightning discharges to the ground. *J. Geophys. Res.*, 84:2439–2456, 1979.

[16] P.R. Krehbiel and R.G. Roble. *The Earth's Electrical Environment.* National Acadmemy Press, 1986.

[17] Y.T. Lin, M.A. Uman, J.A. Tiller, R.D. Brantley, and W.H. Beasley. Characterization of lightning return stroke electric and magnetic fields from simultaneous two-station measurements. *J. Geophys. Res.*, 84(C10).

[18] D.R. MacGorman and W.D. Rust. *The Electrical Nature of Thunderstorms.* Oxford University Press, 1998.

[19] D.M. Mach and W.D. Rust. Two-dimensional speed and optical ristetime estimates for natural and triggered dart leaders. *J. Geophys. Res.*, 102(D12):13,673–13,684, 1997.

[20] W.A. Macky. Some investigations on the deformation and breaking of water drops in strong electric fields. *Proc. Roy. Soc. A*, 133:565–587, 1931.

[21] Thomas C. Marshall and Maribeth. Stolzenburg. Voltages inside and just above thunderstorms. *J. Geophys. Res.*, 106(D5):4757–4768, 2001.

[22] M.J. Master and M.A. Uman. Transient electric and magnetic fields associated with establishing a finite electrostatic dipole. *Am. J. Phys.*, 51.

[23] C.B. Moore, B. Vonnegut, and D.N. Holden. Anomolous electric fields associated with clouds growing over a source of negative space charge. *J. Geophys. Res.*, 94(13):127–134, 1989.

[24] A. Nag, T. Dimitris, V. Rakov, J. Howard, C. Biagi, D. Hill, M. Uman, and D. Jordon. Fine structure of electric field waveforms recorded at near and far distances from the lightning channel. *IEEE Proc. of the Asia-Pacific Int. Symp. of Electr. Comp.*, pages 1,231–1,234, 2010.

[25] C.A. Nucci, C. Mazzetti, F. Rachidi, and M. Ianoz. On lightning return stroke models for lemp calculations. *Proc. 19th Int. Conf. Lightning Protection, Graz, Austria*, 1988.

[26] P.P. Pathak. Positive corona streamer as a source of high-frequency radiation. *J. Geophys. Res.*, 99(D5):10,843–10,845, 1979.

[27] X. Qie, Q. Zhang, Y. Zhou, G. Geng, Zhang T., J. Yang, X. Kong, Q. Xiao, and S. Qu. Artificially triggered lightning and its characteristic discharge parameters in two severe thunderstorms. *Sci. China D-Earth Sci.*, 50(8):1,241–1,250, 2007.

[28] J. Rai, M. Rao, and B.A.P. Tantry. Bremsstrahlung as a possible source of uhf emissions from lightning. *Nature*, 238:59–60, 1972.

[29] V. Rakov and M. Uman. Waveforms of first and subsequent leaders in negative lightning flashes. *J. Geophys. Res.*, 95(D10):16,561–16,577, 1990.

[30] V.A. Rakov and A.A. Duzlon. Calculated electromagnetic fields of lightning return stroke. *Tekh. Elektrodinam.*, 1:87–89, 1987.

[31] Vladamir A. Rakov and Yoshihiro Baba. *Lightning: Principles, Instruments and Applications*. Springer, 2009.

[32] Vladamir A. Rakov and Martin A. Uman. *Lightning Physics and Effects*. Cambridge, Cambridge, third edition, 2005.

[33] M. Rao and H. Bhattacharya. Lateral corona currents from the return stroke channel and the slow field change after the return stroke in a lightning discharge. *J. Geophys. Res.*, 71(11):2811–2813, 1966.

[34] Bill Rison. Nmt course notes for ee 389, spring 2008, 2008.

[35] C.P.R. Saunders, H. Hickson, M.D. Malone, and J. von Richtofen. Charge separation during the fragmentation of rime and frost. *Atmos. Res.*, 29:261–270, 1993.

[36] B.F.J. Schonland. The lightning discharge. *Encyclopaedia of Physics*, pages 576–628, 1956.

[37] S. Soula and S. Chauzy. Charge transfer by precipitation between thunderclouds and ground. *J. Geophys. Res.*, 102:11061–11069, 1997.

[38] K.M.L. Srivastava. Return stroke velocities of a lightning discharge. *J. Geophys. Res.*, 71(4):1283–1286, 1966.

[39] V. Thottappillil R., Rakov and M.A. Uman. Distribution of charge along the lightning channel: relation to remote electric and magnetic fields and to return-stroke models. *J. Geophys. Res.*, 102, 1997.

[40] M.A. Uman and D.K. McLain. Magnetic field of the lightning return stroke. *J. Geophys. Res.*, 74:6899–6910, 1969.

[41] Martin A. Uman. *The Lightning Discharge.* Dover, Mineola, New York, 2001.

[42] J.R. Wait. On the waveform of a radio atmospheric at short ranges. *Proc. IRE*, 44:1052, 1956.

[43] W.P. Winn, G.W. Schwede, and C.B. Moore. Measurements of electric fields in thunderclouds. *J. Geophys. Res.*, 79:1761–1767, 1974.

[44] X. Yang, Q. Zhang, Y. Zhou, G. Geng, Zhang T., J. Yang, X. Kong, Q. Xiao, and S. Qu. Characteristics of channel base currents and close magnetic fields in triggered flashes in shatle. *J. Geophys. Res.*, 115(D231-2):1–12, 2010.